Simulations of particle-driven gravity currents using Eulerian and Lagrangian description

Simulations of particle-driven gravity currents using Eulerian and Lagrangian description

Oliver Häuselmann

Student of Mechanical Engineering

Master's thesis FS2010

Institute of Fluid Dynamics
ETH Zürich

written at

ETH Zürich
Institute of Fluid Dynamics
Zürich, Switzerland

Tutor: R. Henniger
Professor: Prof. Dr. L. Kleiser

Abstract

We perform two dimensional direct numerical simulations of particle-driven gravity currents in a lock-exchange configuration. The fluid is described in an Eulerian framework, whereas the particles are tracked in a Lagrangian manner. The study is restricted to small, monodisperse particles in dilute suspensions, allowing to neglect particle-particle interactions and the particle mass in the continuity equation. The momentum equations for the fluid and for the particles are two-way coupled, whereas the feedback forces of the particles on the fluid are modeled as point forces. We have considered both, particles with and without inertia. Further, we also perform simulations describing the particles as a number density in an Eulerian framework for validation purposes. We evaluate the front position, the mass of suspended particles, the particle deposit and the energy budget of the system. All parameters are chosen such to match the lock-exchange simulations by Necker [8] as close as possible.

Contents

Notation

Roman Symbols

c_p^r	number of real particles per unit area
E	energy
Fr	Froude number
G	generic filter function
g	gravity
g'	reduced gravity
K	kinetic energy of the fluid
K_p	kinetic energy of the particles
l	reference length
L	domain lengths
m	total mass in the domain
M	ratio of real to computational particles
n_p	number of particles
PPC	averaged number of particles per cell in the reservoir
Q_p	kinetic energy leaving the domain due to settling particles
r	radius
Re	Reynolds number
Ri	Richardson number
St	Stokes number
t	time
u	fluid velocity
v	dispersed phase velocity
V	volume
w_p	function which equals unity within a particle
$\boldsymbol{x}$	fluid position vector
$\boldsymbol{y}$	particle position vector

Greek Symbols

δ	Kronecker delta or Dirac delta function
ϵ	dissipation rate
ϕ	volume fraction
μ	dynamic viscosity
ν	kinematic viscosity
ρ	density
τ	timescale
Ω	domain

Superscripts

c	computational
r	real

s	suspension reservoir

Subscripts

0	initial
1, 2, 3	coordinate directions
b	buoyancy
c	cell
d	dissipated by the resolved fluid scales
f	front
K	Kolmogorov
pot	potential
ref	reference
res	reservoir
s	settling / dissipated by microscopic Stokes flow
p	particle

Accents

$\tilde{}$	dimensional

1 Introduction

Particle-driven gravity currents are a special class of gravity currents where the density difference stems from a differential loading of particles [9]. The driving force is the Boussinesq force of the suspended particles which have a higher density than the carrier fluid. Typical examples of particle-driven gravity currents in geophysical situations are turbidity currents in lakes and oceans and powder snow avalanches [8]. Turbidity currents play an important role in erosion processes and sediment transport, whereas snow avalanches are a safety issue. In both cases, prediction of the speed and the run-out length of the current are of practical interest [9]. Often, simplified integral models or theoretical approaches are used for such predictions, and often these models and approaches contain empirical tuning parameters which are determined from comparison with laboratory experiments of prototype configurations [9]. Whereas the front-speed and the height of particle-driven gravity currents can be monitored relatively easy in experiments, detailed features such as the velocity and the particle distribution within the front are difficult to measure accurately [9].

To get a more circumstantial insight into the front, Necker [8] has performed high-resolution simulations resolving all turbulent scales of particle-driven gravity currents in a plane channel. He considers small particles with negligible inertia in dilute suspensions. This allows to treat the particulate phase as a particle-number density with the velocity given by the fluid velocity superimposed by the constant settling velocity in the direction of gravity. As the velocity field of the fluid is divergence free due to incompressibility, the velocity field of the particulate phase is divergence free as well, obviating the accumulation of particles. The feedback force of the particulate phase on the fluid is modeled with the Boussinesq approximation. Due to the usage of a constant settling velocity for the particulate phase relative to the fluid velocity, the analysis is limited to particles with very small Stokes numbers.

Bosse [3] has performed direct numerical simulations (DNS) of dilute, heavy particles settling in homogeneous turbulence, whereas the particles are treated in a Lagrangian manner. The focus of the study is on the effects of two-way coupling on the turbulence modulation and on the enhancement of the particle settling velocity. The latter has been shown to be under-predicted in the one-way coupling case when compared to experimental data [1] [3]. Bosse [3] has found that for a particle-fluid combination with $St \approx 1$ and $\left(\tilde{\rho}_p/\tilde{\rho}\right) \sim 10^3$, a turbulence modification can be observed for particle volume fractions $\phi \gtrsim 10^{-5}$ [3].

In this thesis, we tie in with the study by Necker [8], in particular with the lock-exchange configuration in a plane channel. The initial situation of the generic problem considered is illustrated in figure 1. To overcome the limitation to very small Stokes numbers, we use a Lagrangian description for the particles as used by Bosse [3].

In section 2, we derive the governing equations of the problem, describe the numerical method and derive the integral quantities such as the energy budget of the domain. In section 3, we present simulation results for particles with negligible inertia using the Eulerian concentration and the Lagrangian particle approach and results for particles with inertia. Section 4 closes with concluding remarks and possible future work.

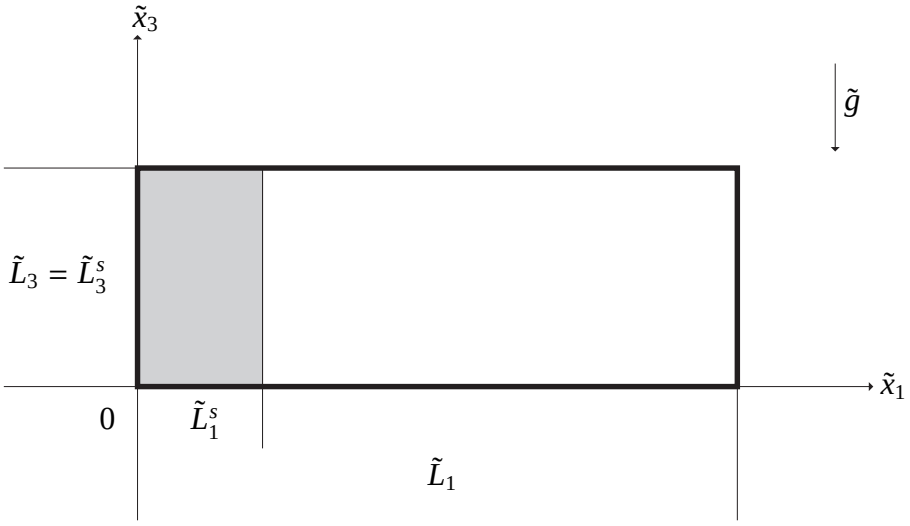

Figure 1: Sketch of the initial situation in a plane channel of length $\tilde{L}_1$, width $\tilde{L}_2$ and height $\tilde{L}_3$. The shaded area illustrates the suspension reservoir (length $\tilde{L}_1^s$, width $\tilde{L}_2^s = \tilde{L}_2$, height $\tilde{L}_3^s = \tilde{L}_3$) filled with particle-laden fluid. The remaining part of the channel contains clear fluid. Gravity acts in the negative $\tilde{x}_3$ direction.

2 Simulation approach

2.1 Governing equations

We consider small (i.e. smaller than the smallest flow scales), spherical, monodisperse particles. We only consider dilute suspensions, so the maximum particle volume fraction never exceeds $\phi_{max} \lesssim 10^{-3}$. This allows to neglect particle-particle interactions [3] [4] and the particle mass in the mass conservation equation, as the coupling between the particle and fluid motion is dominated by the transfer of momentum rather than volumetric displacement effects [8]. The mass conservation equation reduces to the continuity equation for an incompressible fluid,

$$\frac{\partial \tilde{u}_i}{\partial \tilde{x}_i} = 0. \tag{2.1}$$

Here, $\tilde{u}_i$ and $\tilde{x}_i$ are the fluid velocity and the coordinate in the i-th direction, respectively, and we make use of the Einstein summation convention. The tilde is used to denote dimensional quantities. The particle forces considered are the buoyancy force due to the density difference and the Stokes drag. Therefore, the momentum equation for each particle becomes

$$\tilde{\rho}_p \frac{\mathrm{d}\tilde{v}_i}{\mathrm{d}\tilde{t}} = \frac{6\pi\tilde{r}\tilde{\mu}}{\tilde{V}_p}\left(\tilde{u}_i - \tilde{v}_i\right) - \tilde{g}\left(\tilde{\rho}_p - \tilde{\rho}\right)\delta_{i3}, \tag{2.2}$$

where $\tilde{\rho}_p$ is the density of the particle, $\tilde{v}_i$ is the particle's velocity in the i-th direction, $\tilde{r}$ and $\tilde{V}_p$ are the particle's radius and volume, respectively, $\tilde{g}$ is the gravitational acceleration, $\tilde{\mu}$ and ρ are the fluid's viscosity and density, respectively, and δ is the Kronecker delta.

By only considering particles which are much smaller than the smallest flow scales, we can treat the feedback forces of the particles on the fluid as point forces [3]. Therefore, the momentum equation for the fluid can be written as

$$\tilde{\rho}\frac{\mathrm{D}\tilde{u}_i}{\mathrm{D}\tilde{t}} = -\frac{\partial \tilde{p}}{\partial \tilde{x}_i} + \tilde{\mu}\frac{\partial^2 \tilde{u}_i}{\partial \tilde{x}_m \partial \tilde{x}_m} - \frac{6\pi\tilde{r}\tilde{\mu}}{\tilde{V}_p}\sum_{j=1}^{n_p^r}\left(\tilde{u}_i - \tilde{v}_{i,j}\right)\tilde{w}_p\left(\tilde{\boldsymbol{x}} - \tilde{\boldsymbol{y}}_{\boldsymbol{j}}\right) \tag{2.3}$$

where $\boldsymbol{x}$ and $\boldsymbol{y_j}$ are the coordinate vectors of the fluid and the j-th particle, respectively, $v_{i,j}$ is the i-th component of the j-th particle's velocity vector and the function $\tilde{w}_p(\tilde{\boldsymbol{\xi}})$ equals unity if $|\tilde{\boldsymbol{\xi}}| \leq \tilde{r}$ and zero otherwise.

By introducing a reference length $\tilde{l}$ and a reference velocity $\tilde{u}_{ref}$, we can non-dimensionalize our conservation equations (2.1), (2.2), and (2.3) by multiplying them by $\tilde{l}/\tilde{u}_{ref}^2$, $\tilde{l}/(\tilde{\rho}_p\tilde{u}_{ref}^2)$, and $\tilde{l}/(\tilde{\rho}\tilde{u}_{ref}^2)$, respectively. Hence, we obtain

$$\frac{\partial u_i}{\partial x_i} = 0, \tag{2.4}$$

$$\frac{\mathrm{d}v_i}{\mathrm{d}t} = \frac{1}{St}\left(u_i - v_i - u_s\delta_{i3}\right), \tag{2.5}$$

and

$$\frac{\mathrm{D}u_i}{\mathrm{D}t} = -\frac{\partial p}{\partial x_i} + \frac{1}{Re}\frac{\partial^2 u_i}{\partial x_m \partial x_m} - \frac{Ri}{u_s}\frac{1}{\phi_0}\sum_{j=1}^{n_p^r}\left(u_i - v_{i,j}\right)w_p\left(\boldsymbol{x} - \boldsymbol{y_j}\right), \tag{2.6}$$

where $w_p(\boldsymbol{\xi})$ equals unity for $|\boldsymbol{\xi}| \leq r$ and zero otherwise, hence is the dimensionless analogon to $\tilde{w}_p$, and we introduce the dimensionless parameters

$$Re = \frac{\tilde{u}_{ref}\tilde{l}}{\tilde{\nu}}, \tag{2.7}$$

$$St = \frac{2}{9}\frac{\tilde{\rho}_p}{\tilde{\rho}}\frac{\tilde{r}^2}{\tilde{\nu}}\frac{\tilde{u}_{ref}}{\tilde{l}}, \tag{2.8}$$

$$Ri = \frac{\tilde{g}'\tilde{l}}{\tilde{u}_{ref}^2}, \text{ and} \tag{2.9}$$

$$u_s = \frac{StRi}{\phi_0(\tilde{\rho}_p/\tilde{\rho})}. \tag{2.10}$$

We use the same characteristic units as Necker [8], namely half the domain height and the buoyancy velocity, i.e.

$$\tilde{l} = \frac{\tilde{L}_3^s}{2} \text{ and} \tag{2.11}$$

$$\tilde{u}_b = \sqrt{\tilde{g}'\tilde{l}}, \tag{2.12}$$

where $\tilde{g}'$ is the reduced gravity defined as

$$\tilde{g}' = \phi_0\frac{\tilde{\rho}_p}{\tilde{\rho}}\left(1 - \frac{\tilde{\rho}}{\tilde{\rho}_p}\right)\tilde{g}. \tag{2.13}$$

ϕ_0 is the initial particle volume fraction in the reservoir. Given our characteristic units, the Richardson number equals unity by definition. But we still keep it in the equations for generality.

As the particles are monodisperse, we can express the particle volume in two different ways, namely as

$$V_p = \frac{4}{3}\pi r^3 \tag{2.14}$$

and

$$V_p = \frac{\phi_0 V_{res}}{n_{p0}^r}. \tag{2.15}$$

These two expressions are equal, and using the relations (2.7) - (2.10) we obtain the initial number of particles in the reservoir for a given particle volume fraction,

$$n_{p0}^r = \frac{3V_{res}}{4\pi\sqrt{\phi_0}}\left(\frac{2ReRi}{9u_s}\right)^{3/2}. \tag{2.16}$$

In order to discretize the feedback force in equation (2.6), we must substitute w_p for a filter function $G(\boldsymbol{\xi})$. We can do this by integrating the feedback force over a cell volume and dividing by the cell volume. As w_p is zero except inside the particle, the velocity difference takes the value of the velocity difference at the position of the particle as the particle is much smaller than the smallest flow scales. The integration of w_p equals the particle volume. The resulting

expression is amended by the desired filter function under the condition, that the filter function G integrated over the domain equals unity. Hence we obtain

$$\frac{\mathrm{D}u_i}{\mathrm{D}t} = -\frac{\partial p}{\partial x_i} + \frac{1}{Re}\frac{\partial^2 u_i}{\partial x_m \partial x_m} - \frac{Ri}{u_s}\frac{V_{res}}{V_c}\frac{1}{n^r_{p0}}\sum_{j=1}^{n^r_p}\left(u_i - v_{i,j}\right) G\left(\boldsymbol{x} - \boldsymbol{y_j}, \boldsymbol{\Delta}\right), \tag{2.17}$$

where V_c is the cell volume, n^r_{p0} the initial number of physical particles in the reservoir, $\boldsymbol{\Delta}$ the filter width vector of the filter function G, and we use relation (2.15) to substitute the particle volume. Our governing equations for particles with arbitrary Stokes numbers are equations (2.4), (2.5), and (2.17).

One part of validating our code is to compare our results to the findings by Necker [8], i.e. to do simulations of particles with negligible inertia, i.e. small Stokes numbers. For this case, the momentum equations for the particles (2.5) and for the fluid (2.17) can be simplified. The homogeneous solution to equation (2.5) for a constant fluid velocity is an exponential decay, and a particular solution is the right hand side set to zero and solved for v_i. The analytical solution becomes

$$v_i = Ae^{-t/St} + u_i - u_s\delta_{i3} \quad \text{for } u_i = const., \tag{2.18}$$

where A is some constant to meet the initial condition. The solution decays exponentially towards the particular solution. If the time constant St is much smaller than the smallest timescale of the flow, the particle's velocity approaches the particular solution much faster than the fluid velocity changes. Thus, for $St \ll 1$, the momentum equation for the particles can be simplified to

$$v_i = u_i - u_s\delta_{i3}. \tag{2.19}$$

Plugging in the expression for the particle velocity (2.19) into the momentum equation for the fluid (2.17) gives us the simplified equation for particles with negligible inertia.

$$\frac{\mathrm{D}u_i}{\mathrm{D}t} = -\frac{\partial p}{\partial x_i} + \frac{1}{Re}\frac{\partial^2 u_i}{\partial x_m \partial x_m} - Ri\frac{V_{res}}{V_c}\frac{\delta_{i3}}{n^r_{p0}}\sum_{j=1}^{n^r_p} G\left(\boldsymbol{x} - \boldsymbol{y_j}, \boldsymbol{\Delta}\right) \tag{2.20}$$

2.2 Numerical method

The governing equations are solved using the IMPACT simulation code by the IFD [7]. IMPACT is a massively parallel incompressible Navier-Stokes solver using high-order finite difference discretization in space on staggered grids. The pressure field is obtained with a multigrid method. The integration in time is performed with a third-order Runge-Kutta scheme for the fluid and the particle equations.

At each sub-timestep the fluid velocity has to be interpolated to the particle position in order to solve equation (2.5) or (2.19). This is done by a trilinear interpolation from the surrounding grid points in the 3D and by bilinear interpolation in the 2D case. The filter function in equations (2.17) and (2.20) is set to the tent function, which for the 1D case in the i-th direction is defined as

$$G_i\left(\xi_i, \Delta_i\right) = \begin{cases} \frac{\Delta_i - |\xi_i|}{\Delta_i}, & \text{if } |\xi_i| \leq \Delta_i \\ 0, & \text{otherwise} \end{cases} \tag{2.21}$$

with the filter width Δ_i in the i-th spatial direction. For higher dimensions, the tent function is obtained by multiplying the 1D tent functions in the according directions. For example, the 3D

tent function can be written as $G(\boldsymbol{\xi}, \boldsymbol{\Delta}) = G_1 \cdot G_2 \cdot G_3$. The filter widths are chosen to be the local grid spacings in the accordant directions. This equates to distributing each particle's feedback force to the surrounding grid points.

As the necessary number of real particles becomes very large ($n^r_{p0} \sim 10^8$), we make use of the concept of computational particles to reduce the required memory and computational time [3]. Each computational particle represents a cloud of real particles and is described by equation (2.5) or (2.19). By introducing the ratio of real to computational particles

$$M = \frac{n^r_p}{n^c_p} = \frac{n^r_{p0}}{n^c_{p0}}, \tag{2.22}$$

we can modify the feedback force in equation (2.17). The sum is then over all computational particles instead of over all real particles. As a computational particle represents M real particles, the feedback force has to be multiplied by M [3]. But this again cancels out if we substitute n^r_{p0} by Mn^c_{p0} in the denominator. Hence we obtain

$$\frac{\mathrm{D}u_i}{\mathrm{D}t} = -\frac{\partial p}{\partial x_i} + \frac{1}{Re}\frac{\partial^2 u_i}{\partial x_m \partial x_m} - \frac{Ri}{u_s}\frac{V_{res}}{V_c}\frac{1}{n^c_{p0}}\sum_{j=1}^{n^c_p}\left(u_i - v_{i,j}\right) G\left(\boldsymbol{x} - \boldsymbol{y_j}\right). \tag{2.23}$$

Elghobashi [5] analytically derived two criteria for the ratio M in the case of isotropic particle-laden turbulence. The first criterion ensures that the point-force approximation correctly represents the local flow properties around a computational particle and gives a restriction for the particle Reynolds number [3].

$$Re_p = \frac{|\tilde{\boldsymbol{u}} - \tilde{\boldsymbol{v}}_j|\tilde{r}}{\tilde{\nu}} = |\boldsymbol{u} - \boldsymbol{v}_j|\left(\frac{9\phi_0 u_s Re}{2Ri}\right)^{1/2} \leq \frac{1}{M} \tag{2.24}$$

The second criterion ensures that the power spectrum of the two-way coupling source term does not deviate from the one due to real particles [3].

$$1 \leq M \leq O\left(\frac{\phi\eta^3}{r^3}\right) \tag{2.25}$$

Here, η is the Kolmogorov length and ϕ the local volume fraction of the particles.

The boundary conditions for the fluid are chosen to be the same as used by Necker [8]. The lateral boundaries (i.e. in the x_1-x_3- and in the x_1-x_3-plane) are described by symmetry boundary conditions. The top and bottom of the domain are treated as no-slip boundaries for the fluid [8]. Particles which cross a boundary are mirrored back into the domain, except at the bottom where they fall out of the domain to model the settling. Resuspension of particles is not taken into account, as at the Reynolds numbers considered in this thesis it is unlikely to happen. This can be shown using the classical Shields criterion [8].

2.3 Integral quantities

We consider the mass of suspended particles m_p, the front position y_f, the particle deposit, and the energy budget. The mass of suspended particles is given normalized with the initial mass of

suspended particles in the reservoir. This is calculated as the number of particles currently in the domain divided by the initial number of particles in the reservoir.

$$\frac{m_p}{m_{p,0}} = \frac{n_p^r}{n_{p0}^r} = \frac{n_p^c}{n_{p0}^c} \tag{2.26}$$

For the front position, we take the maximum x_1 position over all computational particles, i.e.

$$y_f = \max_{1 \le j \le n_p^c} y_{1,j}. \tag{2.27}$$

The particle deposit is evaluated by distributing a settling particle to the surrounding grid points at the bottom with a 2D tent function.

The energy budget for particle-driven gravity currents consists of the kinetic energy of the fluid K, the potential and kinetic energy of the particles E_{pot} and K_p, respectively, the dissipated energy of the resolved flow scales E_d, and the dissipated energy of the microscopic Stokes flow around the particles E_s. The kinetic energy of the fluid is defined as

$$\tilde{K} = \frac{1}{2}\tilde{\rho} \int_\Omega \tilde{u}_i \tilde{u}_i \mathrm{d}\tilde{V}, \tag{2.28}$$

where Ω is the entire domain. We non-dimensionalize this by dividing by $\tilde{\rho}\tilde{u}_b^2\tilde{l}^3$ and obtain

$$K = \frac{1}{2} \int_\Omega u_i u_i \mathrm{d}V. \tag{2.29}$$

The dimensional potential energy of the particles is defined as

$$\tilde{E}_{pot} = \sum_{j=1}^{n_p^r} \left(\tilde{\rho}_p - \tilde{\rho}\right) \tilde{V}_p \tilde{g} \tilde{y}_{3,j}. \tag{2.30}$$

After non-dimensionalizing and by using the definition of the Richardson number (2.9) and the expression for the particle volume in the monodisperse case (2.15), we get

$$E_{pot} = \frac{RiV_{res}}{n_{p0}^r} \sum_{j=1}^{n_p^r} y_{3,j}. \tag{2.31}$$

The dimensional kinetic energy of the particles within the domain is defined as

$$\tilde{K}_p = \frac{1}{2} \sum_{j=1}^{n_p^r} \tilde{\rho}_p \tilde{V}_p \tilde{v}_{i,j} \tilde{v}_{i,j}. \tag{2.32}$$

By using the definition of the settling velocity (2.10) and the expression for the particle volume in the monodisperse case (2.15), we get

$$K_p = \frac{1}{2}\frac{St}{u_s}\frac{RiV_{res}}{n_{p0}^r} \sum_{j=1}^{n_p^r} v_{i,j} v_{i,j}. \tag{2.33}$$

For negligible particle inertia, the kinetic energy of the particles vanishes, i.e. it is neglected if equation (2.19) is solved instead of (2.5).

The dissipated energy components E_d and E_s are derived by summing up the derivatives of K, E_{pot}, and K_p with respect to time. Some terms cancel each other out, showing that one form of mechanical energy is converted to another. The remaining terms are the derivatives of E_d and E_s. Taking the derivative of K and using the momentum equation (2.17) to substitute the derivative of u_i, we obtain

$$\begin{aligned}\frac{\mathrm{d}K}{\mathrm{d}t} &= \frac{1}{2}\frac{\mathrm{d}}{\mathrm{d}t}\int_\Omega u_i u_i \mathrm{d}V \\ &= \int_\Omega u_i \frac{\partial u_i}{\partial t}\mathrm{d}V \\ &= -\underbrace{\int_\Omega \frac{2}{Re} s_{kl} s_{kl} \mathrm{d}V}_{\varepsilon(t)} + \frac{RiV_{res}}{n^r_{p0} u_s}\sum_{j=1}^{n^r_p}\left(u_{i,j}v_{i,j} - u_{i,j}u_{i,j}\right),\end{aligned} \tag{2.34}$$

where s_{kl} is the rate of strain tensor

$$s_{kl} = \frac{1}{2}\left(\frac{\partial u_k}{\partial x_l} + \frac{\partial u_l}{\partial x_k}\right), \tag{2.35}$$

and ε is the dissipation rate of the resolved flow flow scales. Hence, we obtain E_d by integrating ε over time,

$$E_d(t) = \int_0^t \varepsilon(\tau)\,\mathrm{d}\tau. \tag{2.36}$$

Taking the derivative of equation (2.31) gives

$$\frac{\mathrm{d}E_{pot}}{\mathrm{d}t} = \frac{RiV_{res}}{n^r_{p0} u_s}\sum_{j=1}^{n^r_p} u_s v_{3,j}, \tag{2.37}$$

and taking the derivative of equation (2.33) and using the particle momentum equation (2.5) to substitute the particles' accelerations gives

$$\frac{\mathrm{d}K_p}{\mathrm{d}t} = \frac{RiV_{res}}{n^r_{p0} u_s}\sum_{j=1}^{n^r_p}\left(u_{i,j}v_{i,j} - v_{i,j}v_{i,j} - u_s v_{3,j}\right). \tag{2.38}$$

The sum of equations (2.34), (2.37), and (2.38) is the total change in mechanical energy and therefore the negative change in thermal energy of the system,

$$\frac{\mathrm{d}\left(K + E_{pot} + K_p\right)}{\mathrm{d}t} = -\varepsilon - \underbrace{\frac{RiV_{res}}{n^r_{p0} u_s}\sum_{j=1}^{n^r_p}\left(u_{i,j} - v_{i,j}\right)\left(u_{i,j} - v_{i,j}\right)}_{\varepsilon_s(t)}. \tag{2.39}$$

Here, ε_s is the dissipation rate of the microscopic Stokes flow around the particles. E_d is obtained by integrating ε_s over time,

$$E_s(t) = \int_0^t \varepsilon_s(\tau)\,\mathrm{d}\tau. \tag{2.40}$$

The time integrations for E_d and E_s are performed with a second-order trapezoidal method.

In the limit of small Stokes numbers, the kinetic energy of the particles is neglected and the dissipation rate ε_s can be simplified using (2.19) to

$$\varepsilon_s = \frac{RiV_{res}}{n^r_{p0} u_s} n^r_p u_s^2. \tag{2.41}$$

We notice, that the only varying quantity in relation (2.41) is the number of particles in the domain. Using equations (2.26) and (2.40), the Stokes dissipation for particles with negligible inertia can be written as

$$E_s(t) = RiV_{res} u_s \int_0^t \frac{m_p(\tau)}{m_{p,0}} \mathrm{d}\tau. \tag{2.42}$$

To assure that the implementation is correct, we check the total change of energy of the system. Here, it is important that we define K_p as the kinetic energy of the particles within the domain in equation (2.32). Hence, the kinetic energy flux of the particles leaving the domain is not included in the above analysis. Physically, this energy is dissipated by the inelastic collision of the particles and the ground. Formally, we define it as a sink term Q_p. If we include this in the energy balance of the system, then the total energy of the system

$$E_{tot} = K + E_{pot} + K_p + E_d + E_s + Q_p \tag{2.43}$$

must be constant over time.

3 Simulations

We only perform 2D simulations due to time limitations, but the 3D case is implemented as well. We choose all parameters to match the lock exchange simulations by Necker [8] as close as possible. All simulations are performed with the following parameters:

$$Re = 2236 \tag{3.1}$$
$$u_s = 0.02 \tag{3.2}$$
$$L_1^s = 1 \tag{3.3}$$
$$L_2^s = L_2 = 1 \tag{3.4}$$
$$L_3^s = L_3 = 2 \tag{3.5}$$
$$\phi_0 = 10^{-4} \tag{3.6}$$
$$n_{p0}^r = 1.869 \cdot 10^8 \tag{3.7}$$

Necker [8] does not explicitly define an initial particle volume fraction due to the concentration transport equation being normalized with the initial concentration in the reservoir. But as particle-particle interactions are neglected, it is implicitly assumed that the volume fraction never exceeds 10^{-3}. As Bosse [3] has observed particle accumulation in homogeneous turbulence resulting in local volume fractions one order of magnitude larger than the initial volume fraction, we have chosen the value $\phi_0 = 10^{-4}$. From a numerical point of view it is desirable to chose the volume fraction as large as possible as the initial number of necessary real particles is proportional to $\phi_0^{-1/2}$, as we can see from equation (2.16). It should be noted that Bosse's observation of particle accumulation is for particles with inertia. For the Eulerian concentration approach with negligible particle inertia, the velocity field of the concentration is divergence free and accumulation can not occur [8]. For the Lagrangian particle approach with negligible particle inertia, it is not possible to argue in the exact same manner as the particles are discrete rather than continuous. But as both approaches aim to describe the same physical situation, we would expect to find less particle accumulation for the Lagrangian approach with negligible particle inertia than for the Lagrangian approach with particle inertia, if any at all. This would allow us to use a larger particle volume fraction in the former case, which would require less real particles. Still we choose the same initial volume fraction for both cases for better comparison.

Unless noted otherwise, we use the same domain length as Necker [8], i.e. $L_1 = 18$. For the grid refinement studies of the particle simulation, we use a shorter domain length of $L_1 = 14$ to save computational time when using finer grid resolutions and smaller ratios of real to computational particles. The grid resolution used for the particle simulation is 2049×513, unless noted otherwise. The grid is stretched in the x_3-direction as illustrated in figure 2 to account for the larger gradients at the top and bottom boundaries.

Given our parameters (3.1) - (3.7), we can estimate an upper boundary for the ratio of real to computational particles M using the criteria (2.24) and (2.25). This estimation should be treated with caution, as the second criterion is derived only for isotropic turbulence. For an estimation using the first criterion, we assume the velocity difference to take the value of the settling velocity u_s. This is exact for particles with negligible inertia, and a rough estimation otherwise.

$$M_1 \lesssim \frac{1}{u_s}\left(\frac{2Ri}{9\phi_0 u_s Re}\right)^{1/2} \simeq 350 \tag{3.8}$$

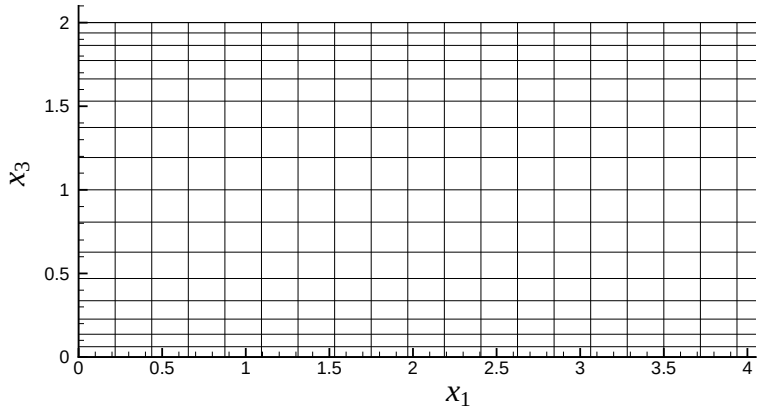

Figure 2: Illustration of the stretched grid.

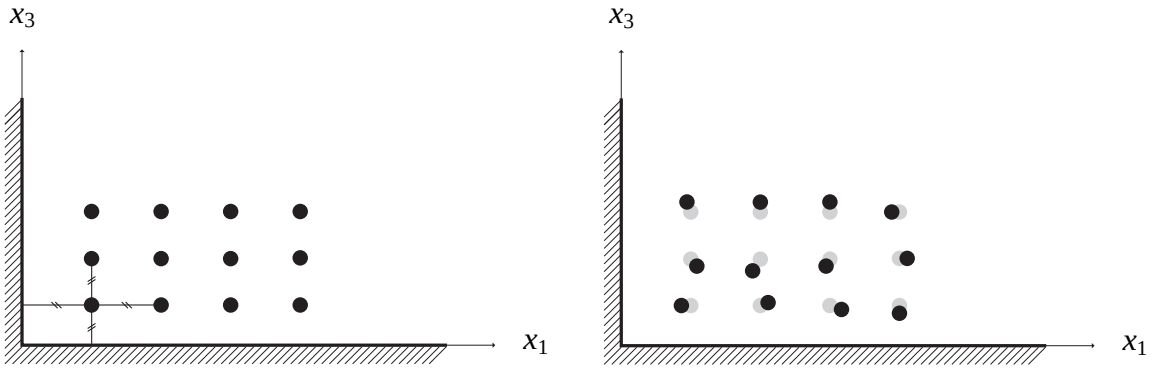

Figure 3: Illustration of the initial particle distribution in the suspension reservoir. Left: Structured on a fixed grid. Right: Structured on a grid superimposed by noise.

For the second criterion, we assume a maximum local particle volume fraction of 10^{-4}, which is the initial volume fraction in the reservoir. For the Kolmogorov scale, we use the two different values 10^{-3} and 10^{-2}, which are a rough estimation of typical grid spacings in the domain as used by Necker [8].

$$M_2 \lesssim O\left(\frac{\phi\eta^3}{r^3}\right) \simeq \begin{cases} O(0.4) & \text{for } \eta = 10^{-3} \\ O(400) & \text{for } \eta = 10^{-2} \end{cases} \tag{3.9}$$

There is a large difference between the two values in equation (3.9), whereas the smaller one would indicate that we could not make use of the concept of computational particles. We use $M = 100$ for most simulations, but also investigate the effect of varying this ratio.

Unless noted otherwise, the particles are initially positioned on a structured grid as illustrated in figure 3. Other initial particle distributions presented are on a structured grid superimposed by noise of controlled maximum amplitude as illustrated in figure 3 and completely random.

The time step limit for the numerical integration is controlled by evaluating the CFL condi-

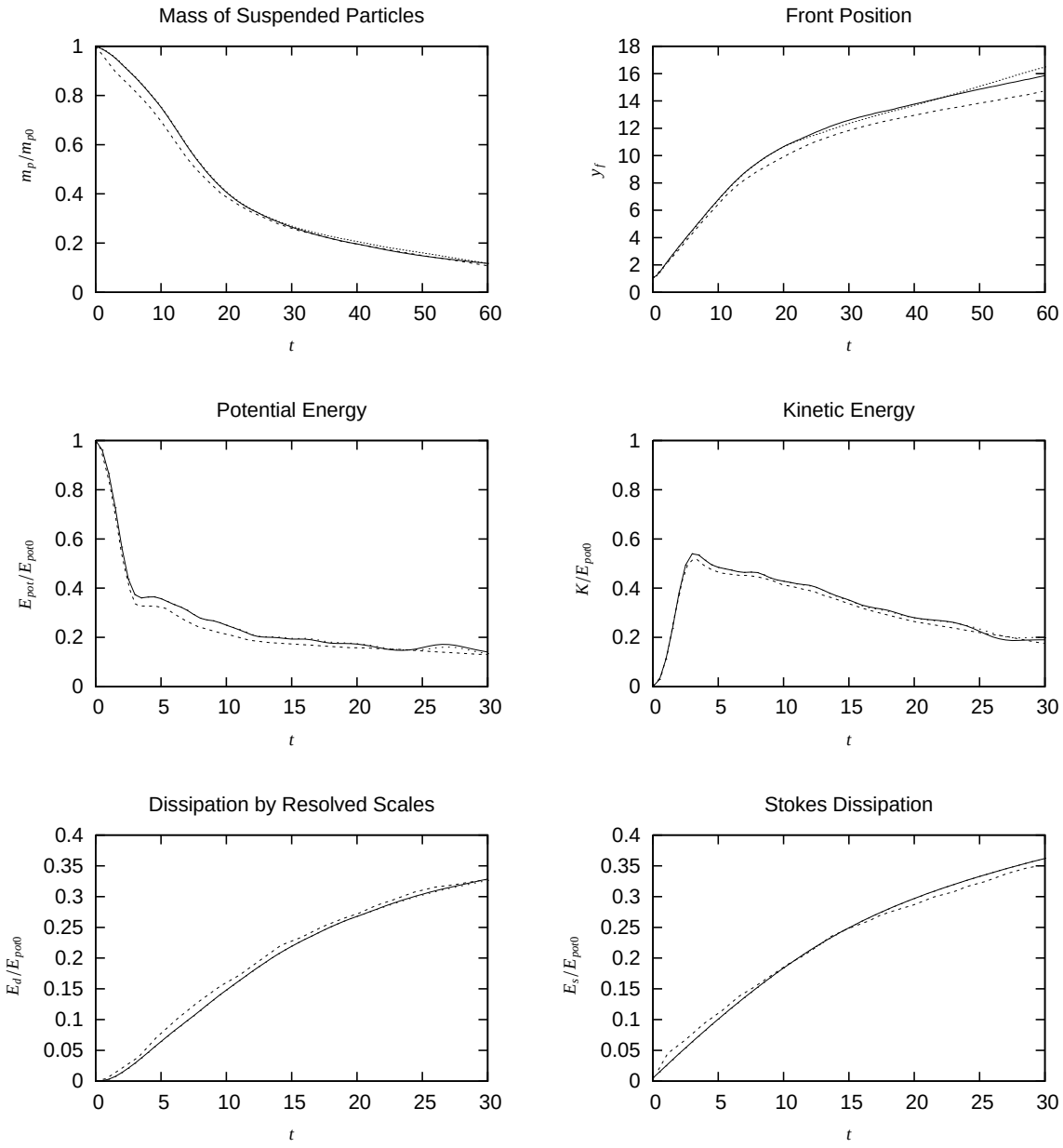

Figure 4: Comparison of the concentration simulations with the IMPACT code with grid resolutions 1025×257 (solid line) and 2049×513 (dots) with the results by Necker [8] (dashed line). All simulations use the parameters (3.1) - (3.5), the Schmidt number $Sc = 1$ and the domain length $L_1 = 18$. The simulation by Necker [8] has a grid resolution of 1440×221.

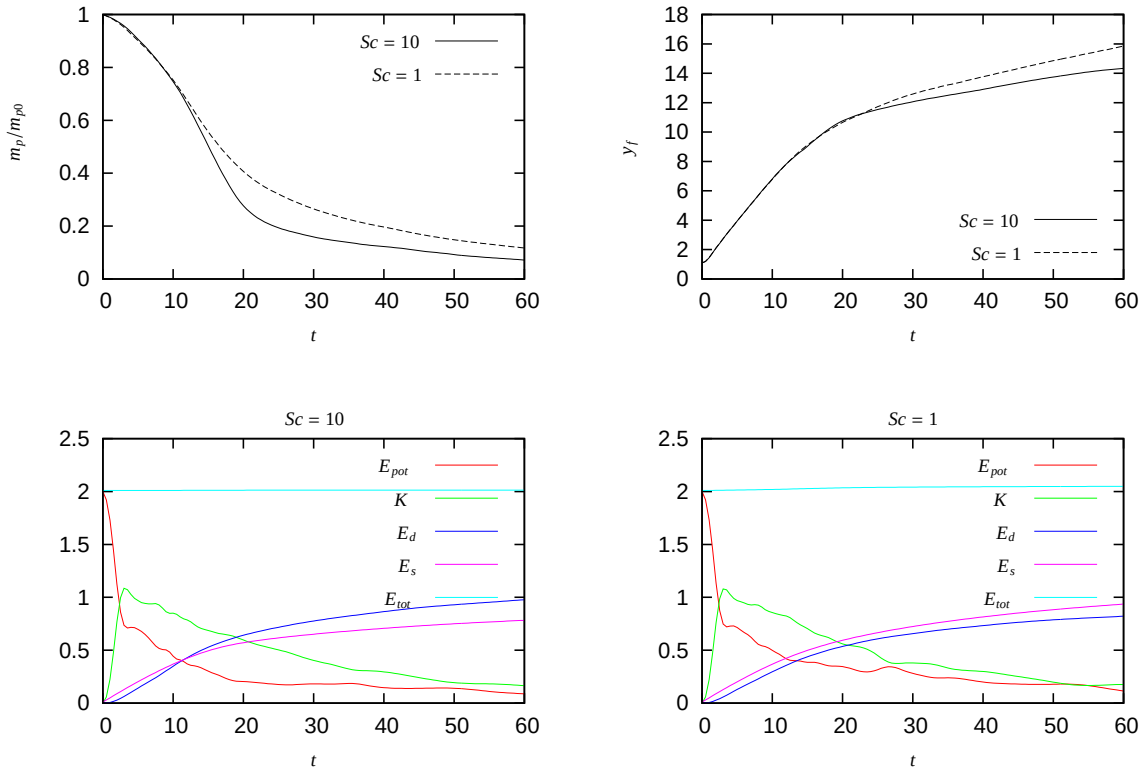

Figure 5: Comparison of the integral quantities of the concentration simulations with $Sc = 10$ (solid line and bottom left) and $Sc = 1$ (dashed line and bottom right).

tion. For particles with negligible inertia, we choose a value of 0.75. For the heavy particles, the time step limit has to be adjusted to assure stability and we use a value of 0.5.

For comparisons of the Lagrangian particles with the Eulerian concentration approach, we also perform simulations with the equations used by Necker [8] with the IMPACT code. Figure 4 compares our results from the Eulerian approach for two different grid resolutions to the ones by Necker [8] for the values given in (3.1) - (3.5) and the Schmidt number $Sc = 1$. The Schmidt number is defined as $Sc = \tilde{\nu}/\tilde{D}$, where $\tilde{D}$ is the diffusion coefficient in the dimensional concentration transport equation. The results for the two simulations with the IMPACT code only show minor deviations in the front position for $t \gtrsim 20$. Apart from that they agree very well, indicating that the grid resolution for the coarser grid suffices. The results by Necker are in good agreement with the results obtained with the IMPACT code. Noticeable differences are that the particles initially settle faster and that the front moves slower for the simulation performed by Necker.

As we do not have any diffusion for the simulations with the Lagrangian particle approach, we also perform concentration simulations with the Schmidt number $Sc = 10$ to investigate the influence of diffusion. As a higher Schmidt number means a lower prefactor for the diffusion term in the concentration transport equation, we choose a finer resolution (2049×513) for the simulation with $Sc = 10$ to resolve the resulting steeper gradients. Figure 5 compares the integral quantities of the simulation with $Sc = 10$ to the simulation with $Sc = 1$. We can see,

that the particles settle faster, the front moves more slowly and the potential energy overall is lower for $Sc = 10$. Further, we see that the dissipation after $t \gtrsim 10$ is dominated by the resolved flow scales rather than by the microscopic Stokes flow around the particles, i.e. $E_d > E_s$ for $t \gtrsim 10$ and $Sc = 10$.

The gain in total energy stems from the diffusion of the solid phase which causes a mean transport of particles in the positive x_3 direction due to the particle concentration mostly being lower for larger values of x_3. This produces potential energy in the system which physically would be compensated by a reduction of thermal energy. We do not take this effect into account for the energy balance. We calculate the total energy gain to be $3.98 \cdot 10^{-3}$ for $Sc = 10$ and $4.30 \cdot 10^{-2}$ for $Sc = 1$. It is lower in the former case as a higher Schmidt number corresponds to a lower diffusion coefficient.

Figures 6 and 7 both show a sequence of contour-plots of the concentration simulations with grid resolution 2025×513 and Schmidt number $Sc = 10$ and $Sc = 1$, respectively. We can see that as the particles move down, the front develops and eventually Kelvin-Helmholtz vortices form. We also see that for the higher Schmidt number $Sc = 10$, there are much finer structures in the Kelvin-Helmholtz vortices than for the lower Schmidt number $Sc = 1$.

We also performed a simulation with $Sc = 10$ and a grid resolution of 4097×1025 up till $t = 20$. A longer simulation was not feasible. We did not observe any difference in the integral quantities to the coarser grid up during this period. For comparisons with the particles, we use the resolution 2049×513 and the Schmidt number $Sc = 10$ for the concentration simulation.

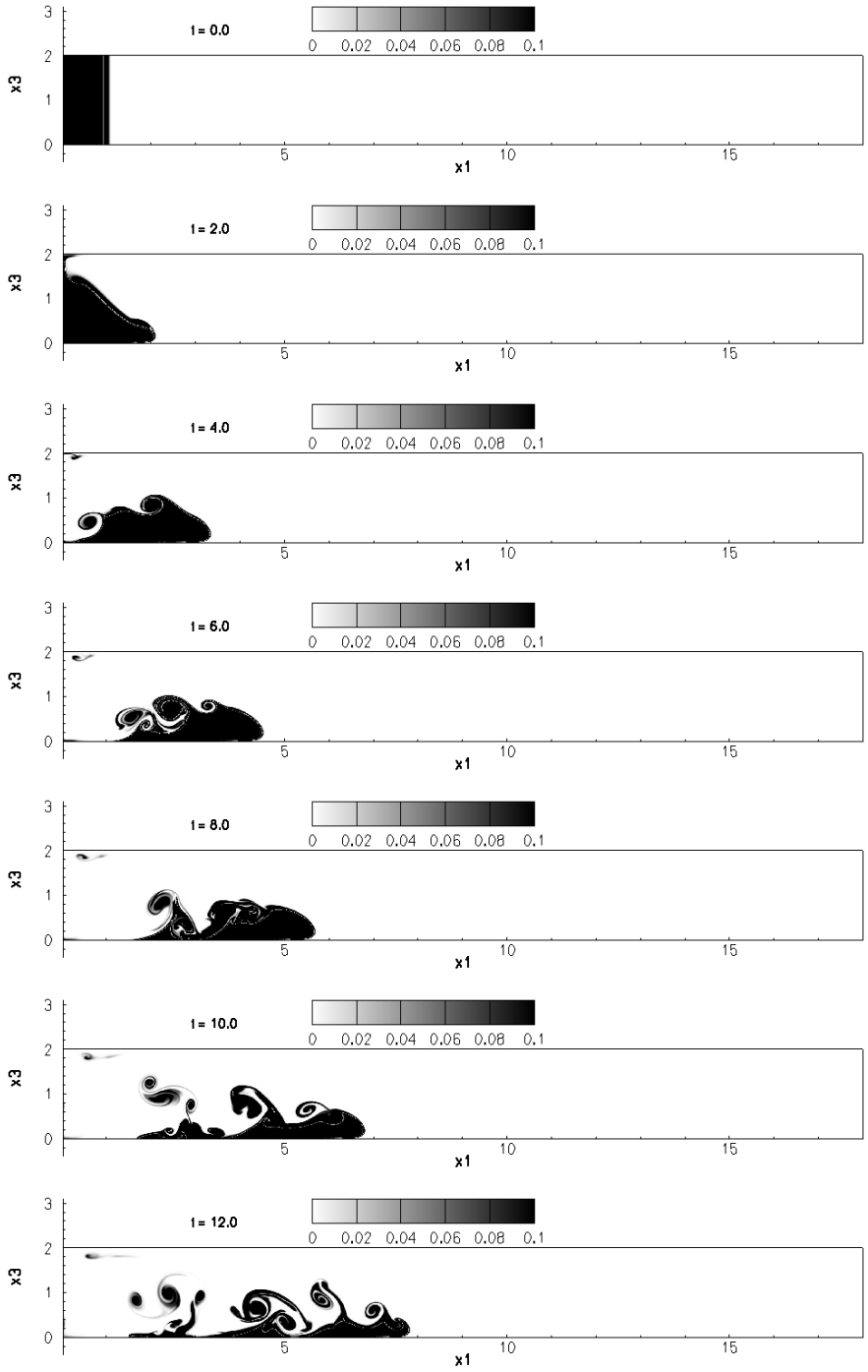

Figure 6: Contour plots of the concentration simulation with $Sc = 10$. The quantity plotted is ϕ/ϕ_0. The plotted range of this value is chosen lower for better comparison with the scatter-plots of the particle simulation.

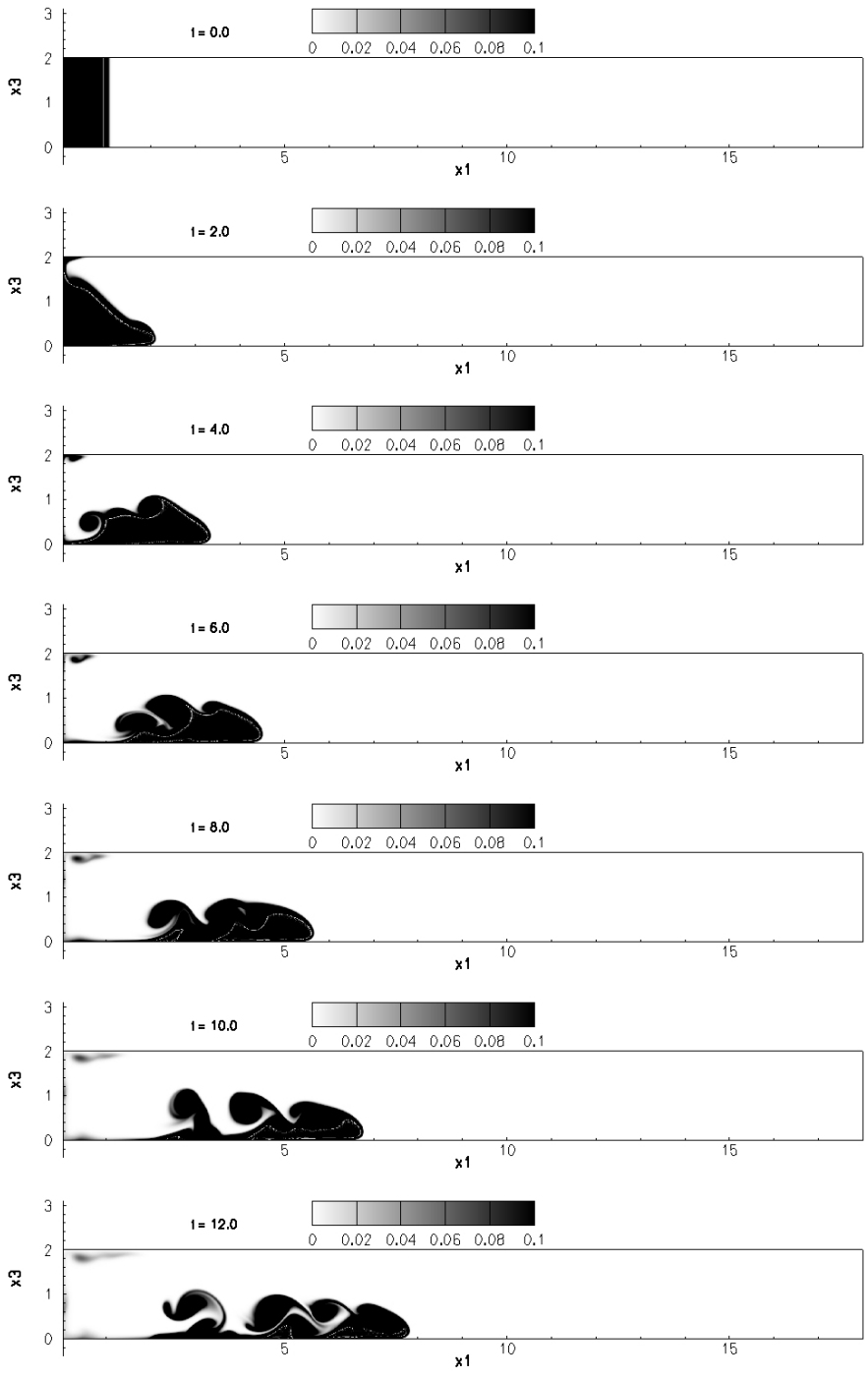

Figure 7: Contour plots of the concentration simulation with $Sc = 1$.

3.1 Particles with negligible inertia

Figure 8 shows a sequence of scatter-plots of a particle simulation. Comparing the particle simulation in figure 8 with the concentration simulation in figure 6, we see a very good agreement in the front position and height and in the formation of the vortices. An agreement in the shape of the vortices is hard to determine due to the nature of the scatter-plots, but there seems to be a qualitative agreement.

Figures 9 and 10 compare the integral quantities of these two simulations in figures 8 and 6. We can observe a faster settlement and a lower front speed for the particle simulation. The curve for the front position of the concentration simulation in figure 10 dips towards the end. This is due to the way we determine the front position in the concentration approach. We take the front position as the maximum x_1 value where the local volume fraction normalized with the initial volume frather in the reservoir exceeds a predefined threshold, which we have chosen as 0.01. Thus the dips in the curve are due to dilution. A further difference we observe is that for the particle simulation, more energy is dissipated by the resolved scales and less by the microscopic Stokes flow around the particles. We can see this in figure 9 where the two curves intersect earlier for the particle simulation than for the concentration simulation and from the final values in figure 10.

These are all differences we also observe in figure 5, where we compare the concentration simulations with $Sc = 10$ and $Sc = 1$. This indicates that the differences in the integral quantities of the particle and the concentration simulation in figures 9 and 10 could be due to our Lagrangian particle approach not containing any diffusion.

To investigate the influence of grid refinement and variation of the ratio of real to computational particles M, we perform six simulations with the domain length $L_1 = 14$ up till $t = 20$. The integral quantities are presented in figure 11. We can observe slight variations as we vary the ratio M, but it is hard to see any regularity. For the finer grid we observe an increase in E_d compared to the coarser one for all M, which we also observed when we refined the grid in the concentration approach. Further, we observe a loss in the total energy of the system. We calculate the relative energy loss of the system at $t = 20$, i.e. $(E_{tot}(20) - E_{tot}(0))/E_{tot}(0)$. For the coarser grid, this energy loss is $6 \cdot 10^{-3}$, and for the finer grid $2 \cdot 10^{-3}$, independent of M. An image sequence of scatter-plots of the simulation with the finest grid and the lowest ratio M is shown in figure 13. Noticeable is that for $t \geq 10$, the shapes of the vortices seem to agree worse with the concentration simulation in figure 6 than the vortices for the particle simulation with the higher ratio M in figure 8.

While testing the code, we have found that the energy loss of the system is an indicator for determining whether the grid resolution and the ratio M are sufficient. Figure 14 shows the relative energy loss at $t = 3$ for very coarse grids and few particles. We can see that the energy loss depends on both, the grid resolution and the number of particles. This indicates that the ratio M was chosen sufficiently, but that the solution might still improve for finer grid resolutions.

The figures 15 and 16 show the deposit at $t = 2, 4, 6, 8, 10$, and 12 and at $t = 5, 10, 20$, and 100, respectively, and the corresponding scatter-plots. The deposit is described in terms of the number density c_p^r defined as the number of real particles per unit area. Looking at figure 15, we see an almost linear decrease in c_p^r for larger values of x_1 for times $t \geq 6$. From this we can conclude that for an undisturbed front, the deposit at a certain position is proportional to the time for which this position has been covered with particles $\Delta t_{covered}$. To illustrate this, we predict the slope of the curves in figure 15. As we do not expect any particle accumulation, we

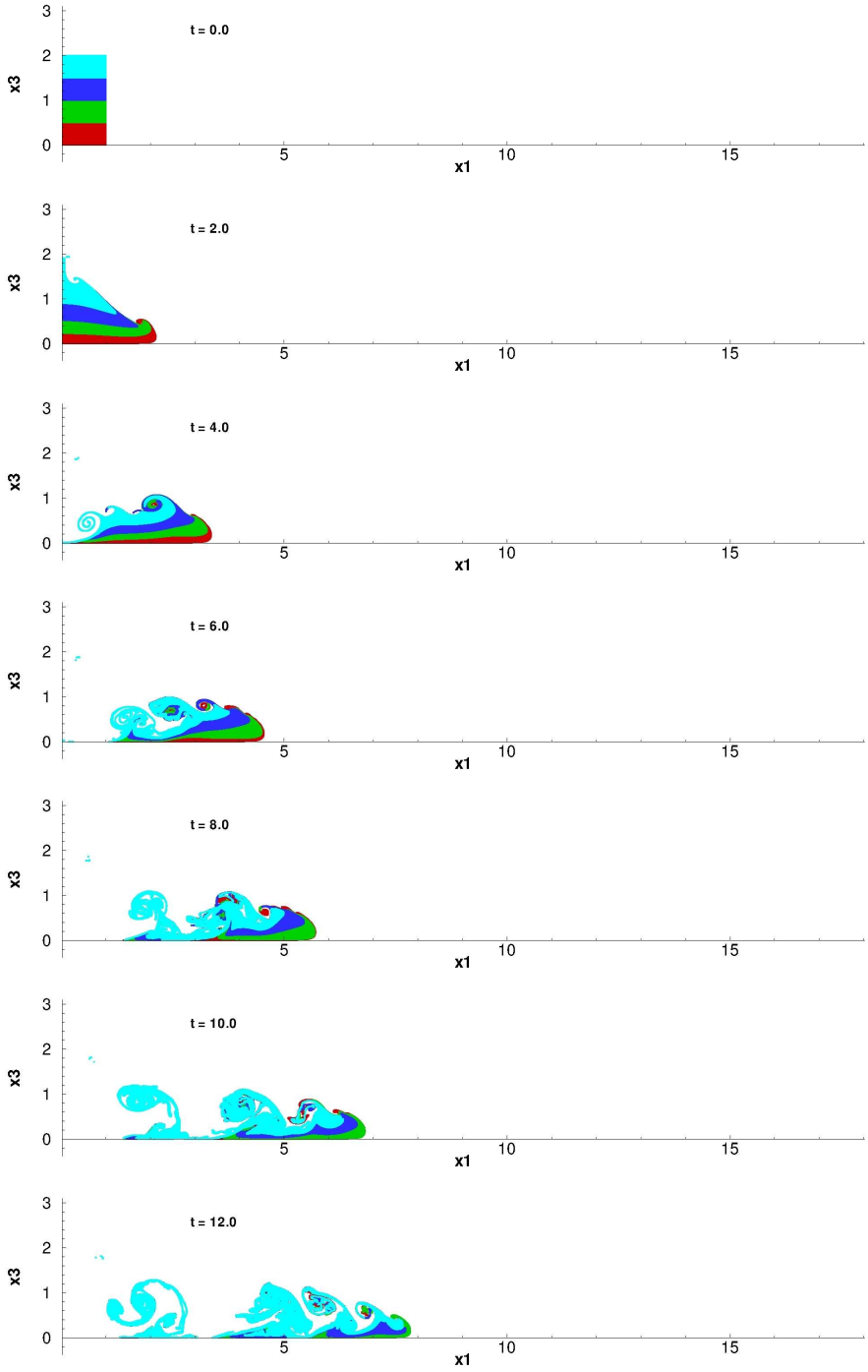

Figure 8: Scatter-plots of particles with negligible inertia with domain length $L_1 = 18$, grid resolution 2049×513 and real to computational particles ratio $M = 100$. The particles are color-coded into four groups depending on their initial position.

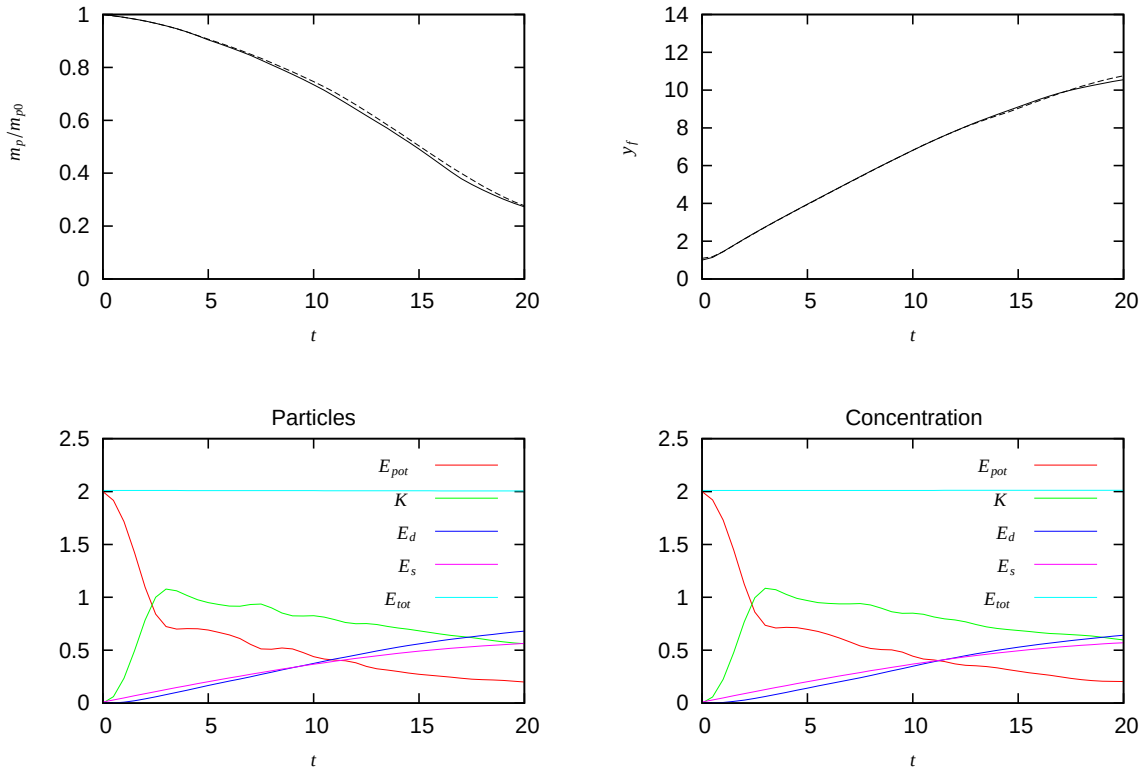

Figure 9: Integral quantities of the particle simulation in figure 8 (solid and bottom left) and the concentration simulation in figure 6 (dashed and bottom right) for $0 \leq t \leq 20$.

assume the volume fraction of the particles within the front to equal the initial volume fraction in the reservoir as long as there is no dilution. And as the fluid can not penetrate the wall, the velocity of the particles at the wall is the constant settling velocity u_s in the negative x_3 direction. So we can write

$$c_p^r(x_1) = \frac{n_{p0}^r}{V_{res}} u_s \Delta t_{covered}(x_1), \tag{3.10}$$

where we use equation (2.15) to convert the volume fraction to a number density. From figure 9, we find an almost constant increase in the front position, i.e. a constant front speed v_f, for $3 \lesssim t \lesssim 12$. From the results of the simulation presented in figure 15, we calculate a mean front speed of $v_f = 0.577$ for the time period $5 \lesssim t \lesssim 10$. For a constant front speed and as long as the considered position remains covered by particles, we can write $\Delta t_{covered}(x_1, t) = (\max(x_{covered}(t)) - x_1)/v_f$, where $\max(x_{covered})$ is the maximum x_1-coordinate covered by particles at time t. This lets us express the derivative of 3.10 as

$$\frac{\partial c_p^r}{\partial x_1} = -\frac{n_{p0}^r}{V_{res}} \frac{u_s}{v_f} = -3.241 \cdot 10^6. \tag{3.11}$$

From the data of the deposit at $t = 10$ in figure 15, we calculate a slope of $-3.244 \cdot 10^6$ for $3.7 \leq x_1 \leq 7.3$, which corresponds to the time period used for the calculation of v_f. For earlier times we can see deviations from this slope as the front is still accelerating, and for the curves

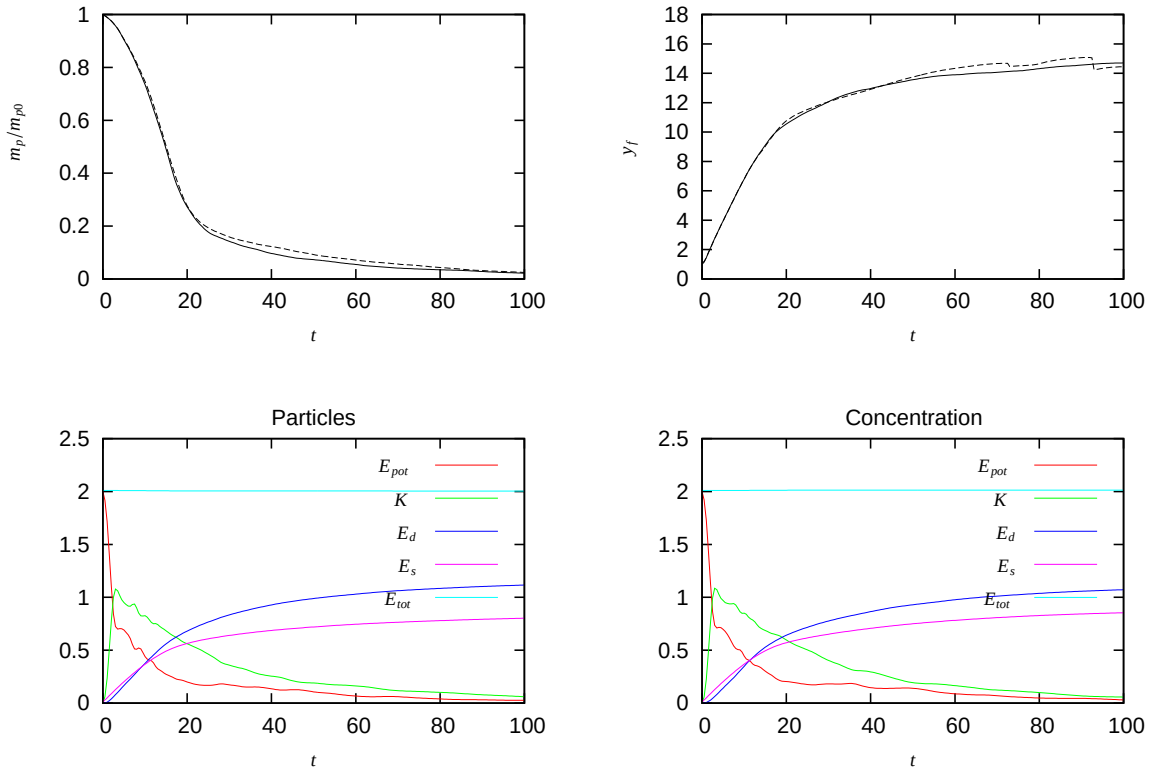

Figure 10: Integral quantities of the particle simulation in figure 8 (solid and bottom left) and the concentration simulation in figure 6 (dashed and bottom right) for $0 \leq t \leq 100$.

at $t = 20$ and $t = 100$ in figure 16 a deviation as the front has slowed down again and dilution occurs. Equation (3.10) also gives us an upper bound for the deposit as the settling velocity is constant and the volume fraction of the particles can never exceed ϕ_0.

For the curves $t \geq 6$ and $t \geq 8$ in figure 15, we can see significant drops in the deposit around $x_1 \approx 1$ and $x_1 \approx 3$, respectively. This is due to the formation of Kelvin-Helmholtz vortices, as we can see in the scatter-plots. These vortices cause an entrainment of clear fluid into the current which dilutes the suspension and hence reduces the deposit. Figure 17 shows the deposit evolution for the particle simulation with $M = 100$, the particle simulation with $M = 50$ and the concentration simulation. The curves for the particle simulation with $M = 100$ are much noisier than for the simulation with $M = 50$. The peak around $x_1 \approx 2$ for $t \geq 8$ is highest for $M = 100$ and lowest for the concentration simulation. This is due to the dip before the peak being narrowest for $M = 100$ and widest for the concentration simulation. The concentration simulation differs from the particle simulations in terms of that the curves flatten as c_p^r approaches zero and that for $t \geq 6$ the small peak right next to the left wall and the following dip are less distinct. These are both regions of low fluid velocity and therefore these differences are probably caused by concentration diffusion. Diffusion is also the reason for the curves being smooth as it evens out the large gradients we get for the noisy sections of the deposits from the particle simulations. Further, the curve for $t = 2$ shows much higher values than the same curves in the particle simulations.

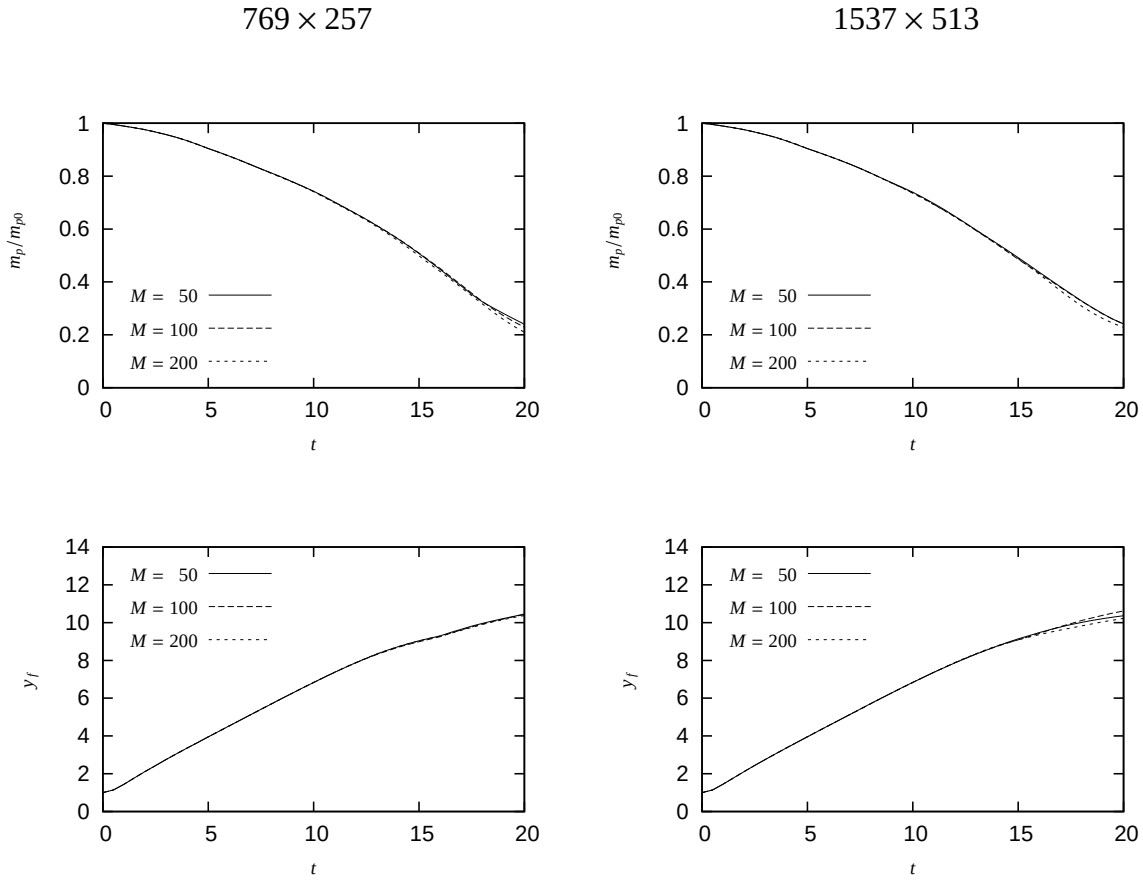

Figure 11: Mass of suspended particles and front position for two different grid resolutions and three different ratios M.

Figure 18 shows the final deposit for the particle and the concentration simulation at $t = 100$. For $x_1 \lesssim 5$, there is a good agreement in the magnitude and shape of the peaks and dips, but they appear a little further downstream for the concentration simulation. For $x_1 \gtrsim 5$, the shapes do not agree as well anymore. Overall the concentration simulation deposits more matter further downstream than the particle simulation, which can be verified by the difference in the mass of suspended particles in figure 10.

The instantaneous findings for the deposits must be treated with care, as the deposit is sensitive to the initial particle distribution. Figure 19 shows two simulations with the particles distributed randomly in the reservoir instead of structured as illustrated in figure 3. From the variation in magnitude and location of the dints and peaks we can conclude that the Kelvin-Helmholtz vortices form at different locations and to a different extent. To gain more detailed insight into the sensitivity, we have performed simulations where we superimposed noise of varying maximum amplitude on the otherwise structured particle positions, as illustrated on the right in figure 3. For $M = 100$, the distance between the particles on the perfectly structured grid is 10^{-3} in both directions, and the amplitude of the noise varies from 10^{-8} to 10^{-3}. These simulations, as well as the reference without noise, are performed with a grid resolution of 1025×257. The final deposits for all simulations at $t = 100$ are shown in figure 20. We can see that all simulations agree with the reference without noise for small values of x_1. Further, we observe that the smaller the noise amplitude, the further the deposit agrees with the reference.

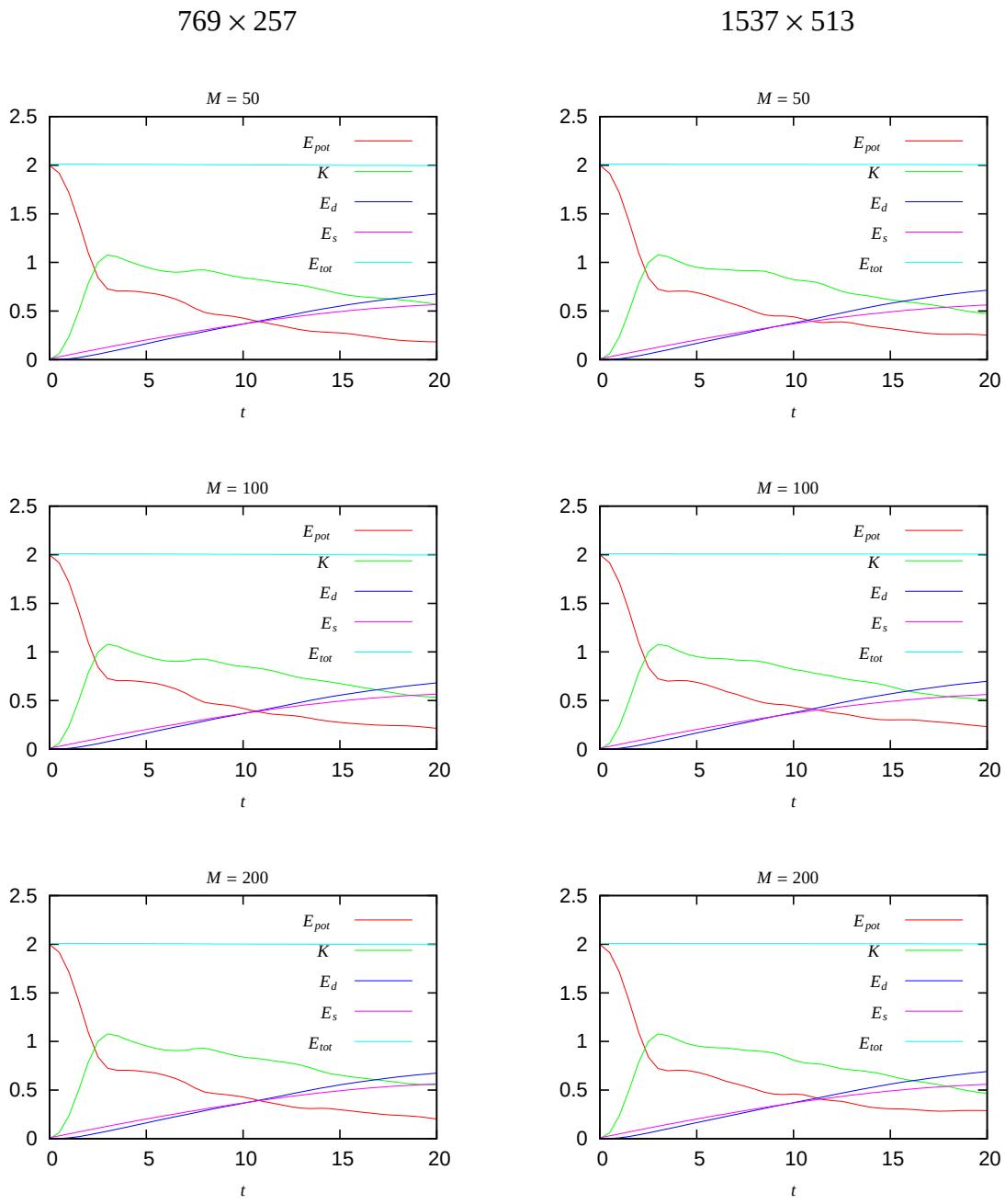

Figure 12: Energy plots for the same simulations as in figure 11.

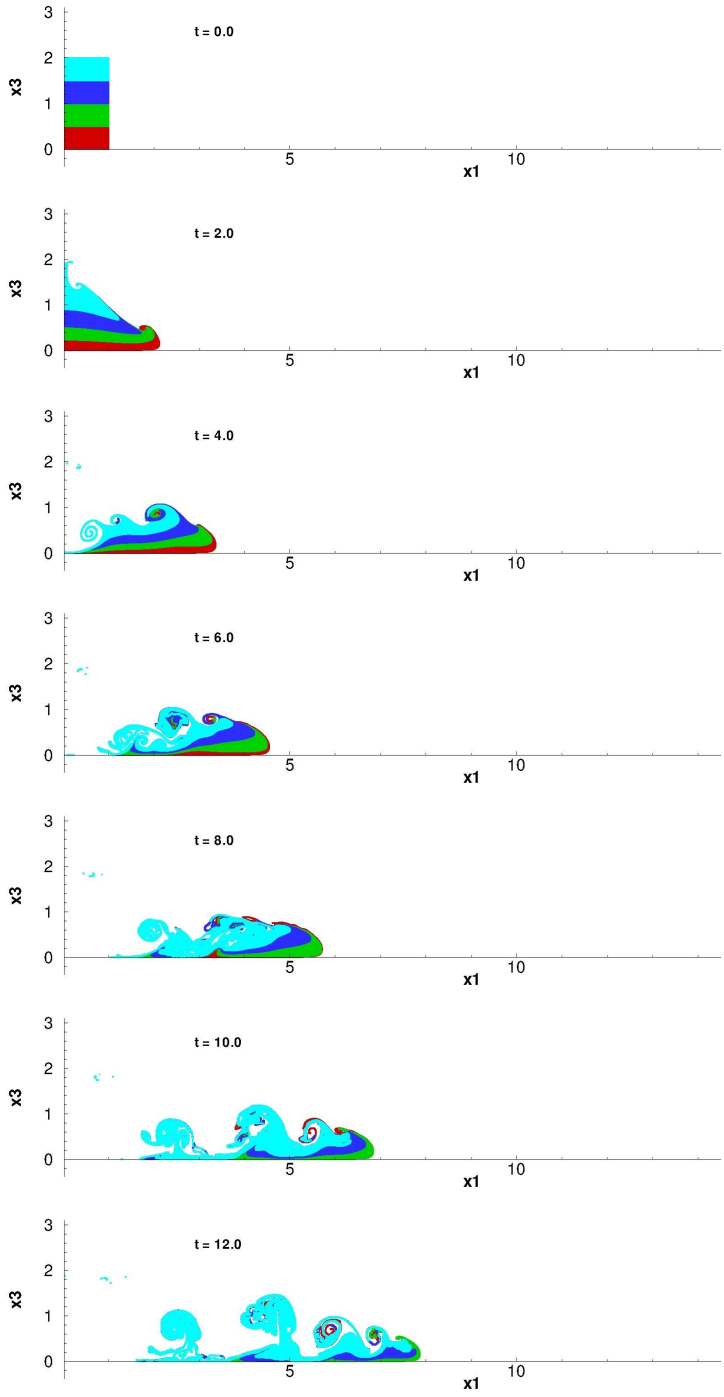

Figure 13: Scatter plots of the simulation with the finest grid (1537x513) and the lowest ratio $M = 50$ from the grid refinement study.

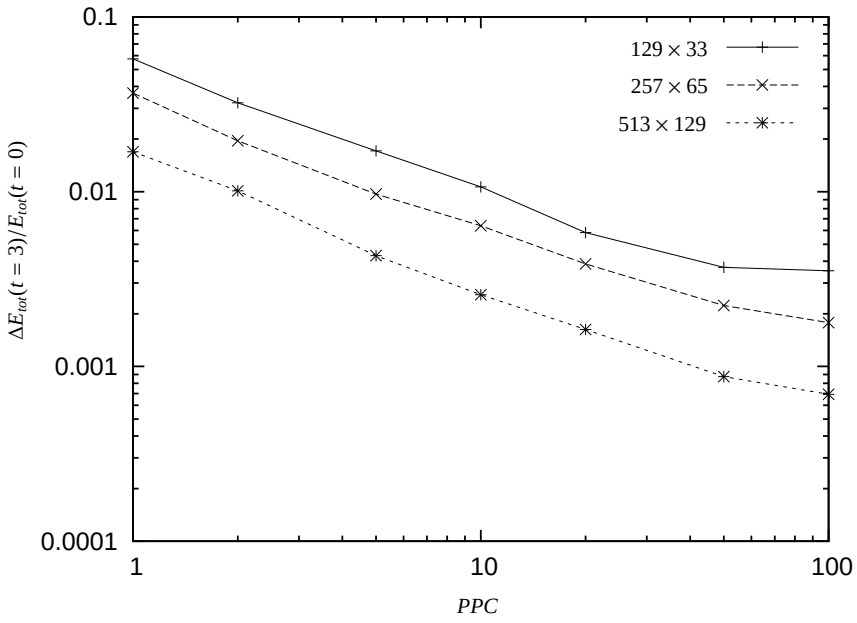

Figure 14: Relative energy loss at $t = 3$ over the average number of particles per cell in the reservoir (*PPC*) for three different grid resolutions.

After the deposits differ substantially from the reference, there is no strict correlation between the noise amplitude and the level of disagreement. The early evolution of the deposit for the simulation with the largest noise amplitude is shown in figure 21. We can see that for the earlier times shown, the deposit agrees well with the reference, and then differs for the later times for $x_1 \gtrsim 2$. Figure 22 shows six selected particle paths for the same simulations as shown in figure 21. We can see that especially the blue and the yellow curve differ significantly for $x_1 \gtrsim 4$.

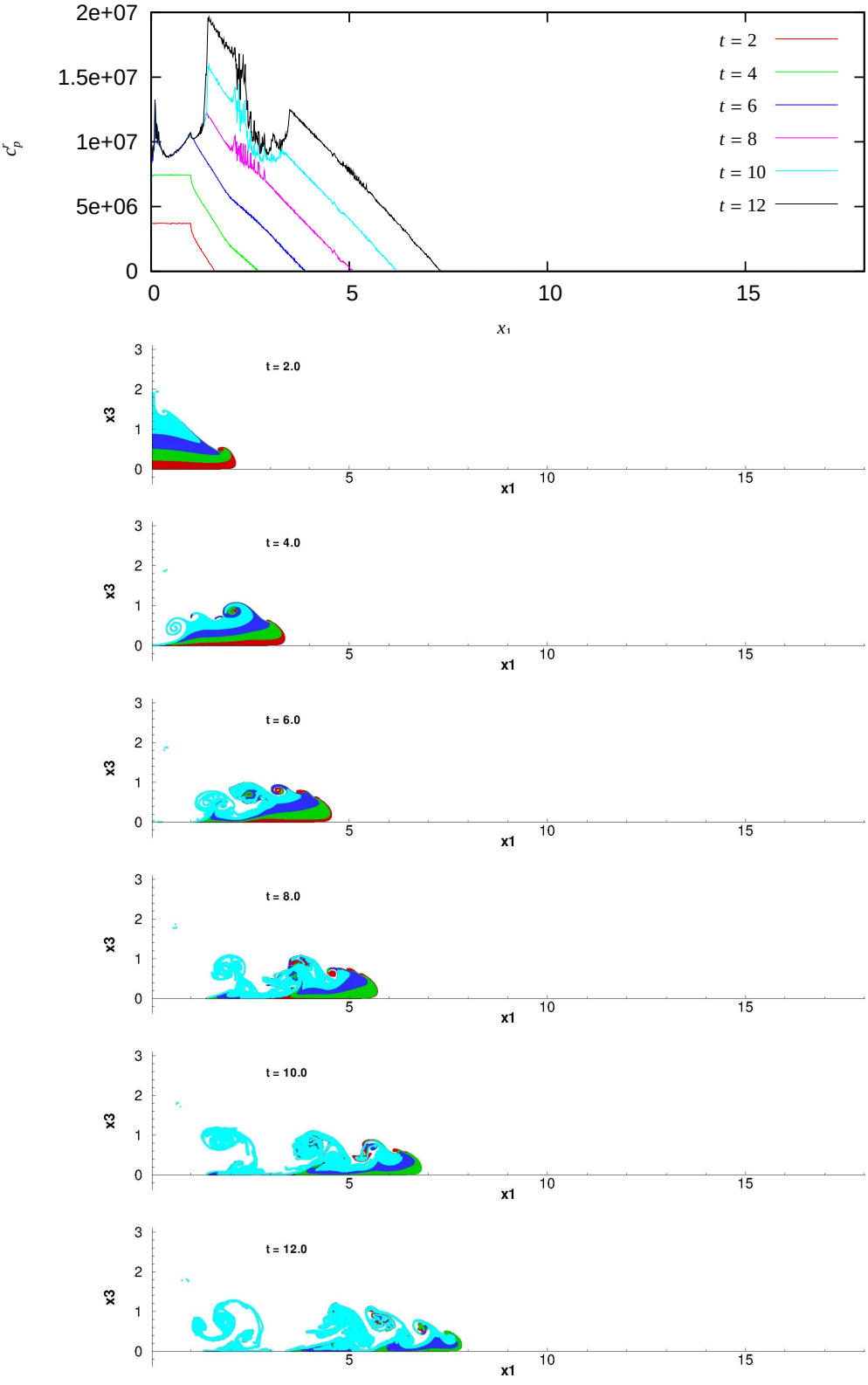

Figure 15: Deposit evolution and corresponding scatter-plots for the particle simulation in figure 8 with grid resolution 2049×513 and $M = 100$.

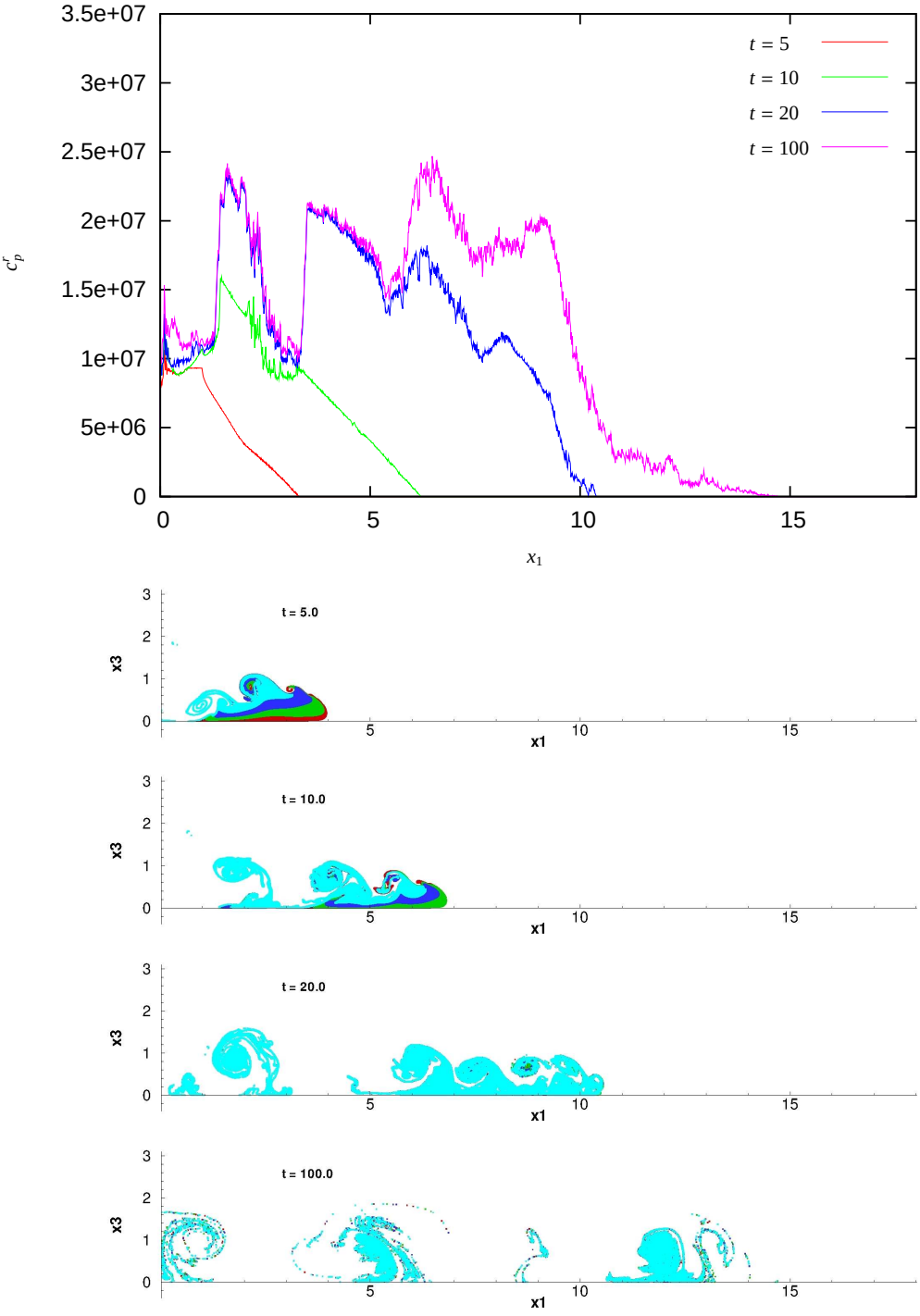

Figure 16: Deposit evolution and corresponding scatter-plots for the particle simulation in figure 8 with grid resolution 2049×513 and $M = 100$.

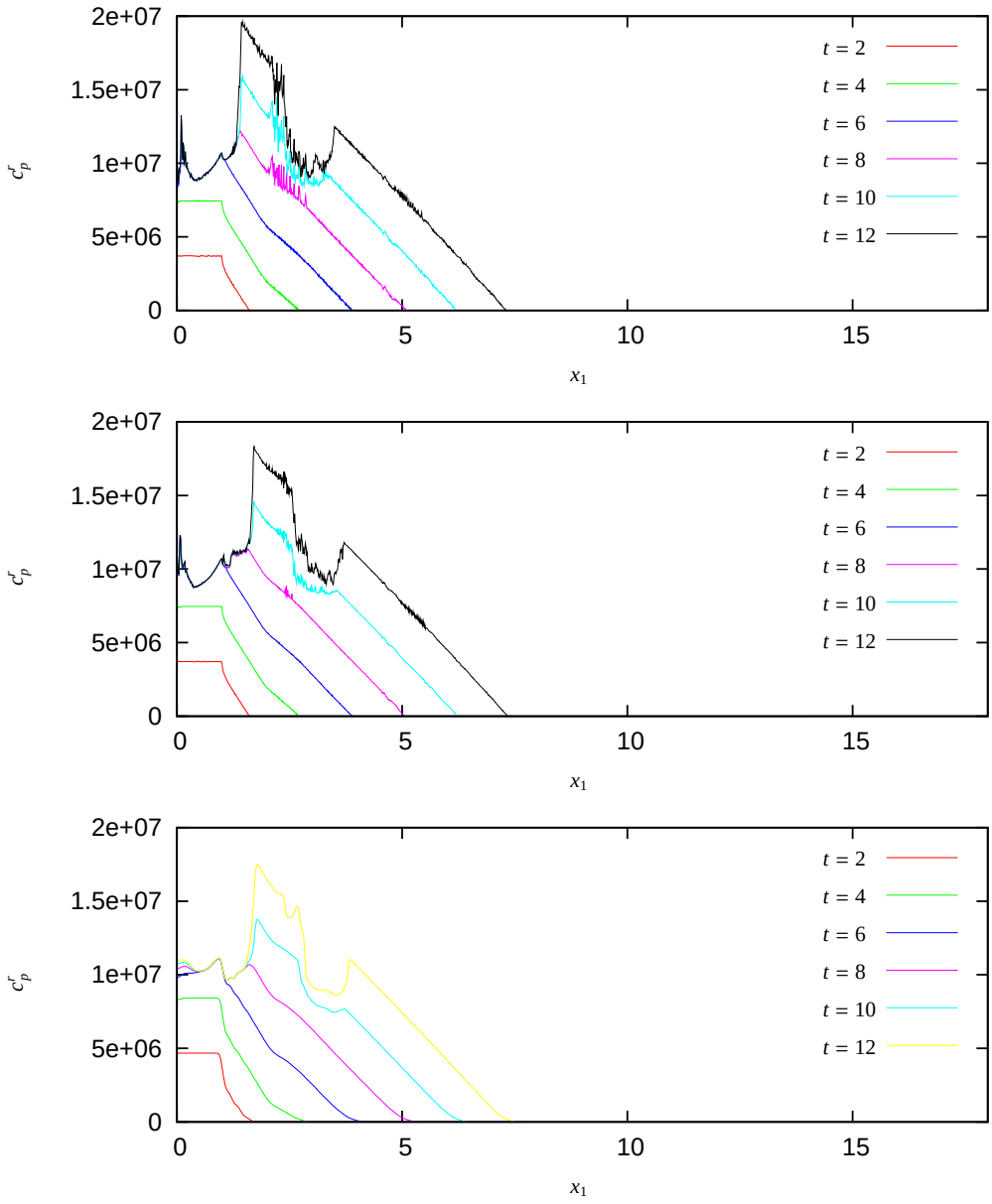

Figure 17: Deposit evolution. Top: Particle simulation with grid resolution 2049×513, domain length $L_1 = 18$ and $M = 100$. Middle: Particle simulation with grid resolution 1537×513, domain length $L_1 = 14$ and $M = 50$. Bottom: Concentration simulation with grid resolution 2049×513 and domain length $L_1 = 18$.

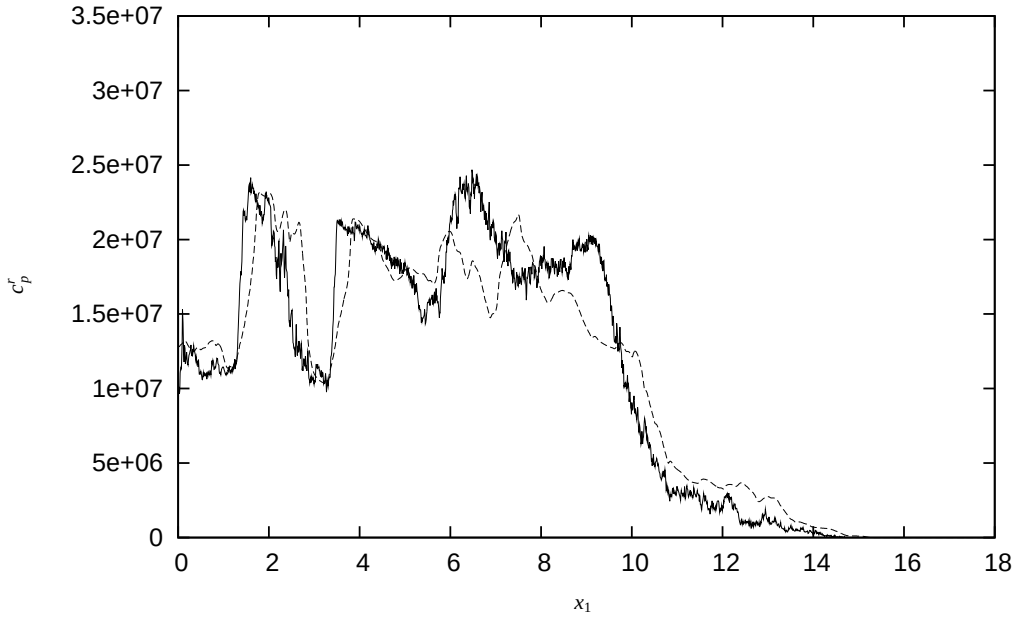

Figure 18: Final deposits at $t = 100$ for the particle (solid) and the concentration (dashed) approach.

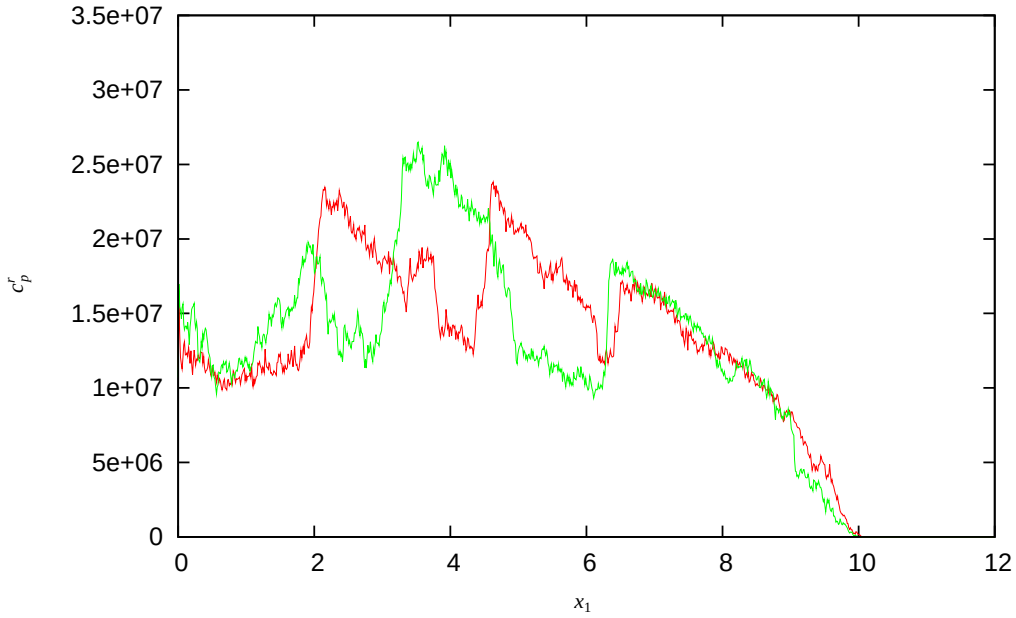

Figure 19: Deposits of two simulations with random initial particle distributions in the reservoir, but otherwise identical settings.

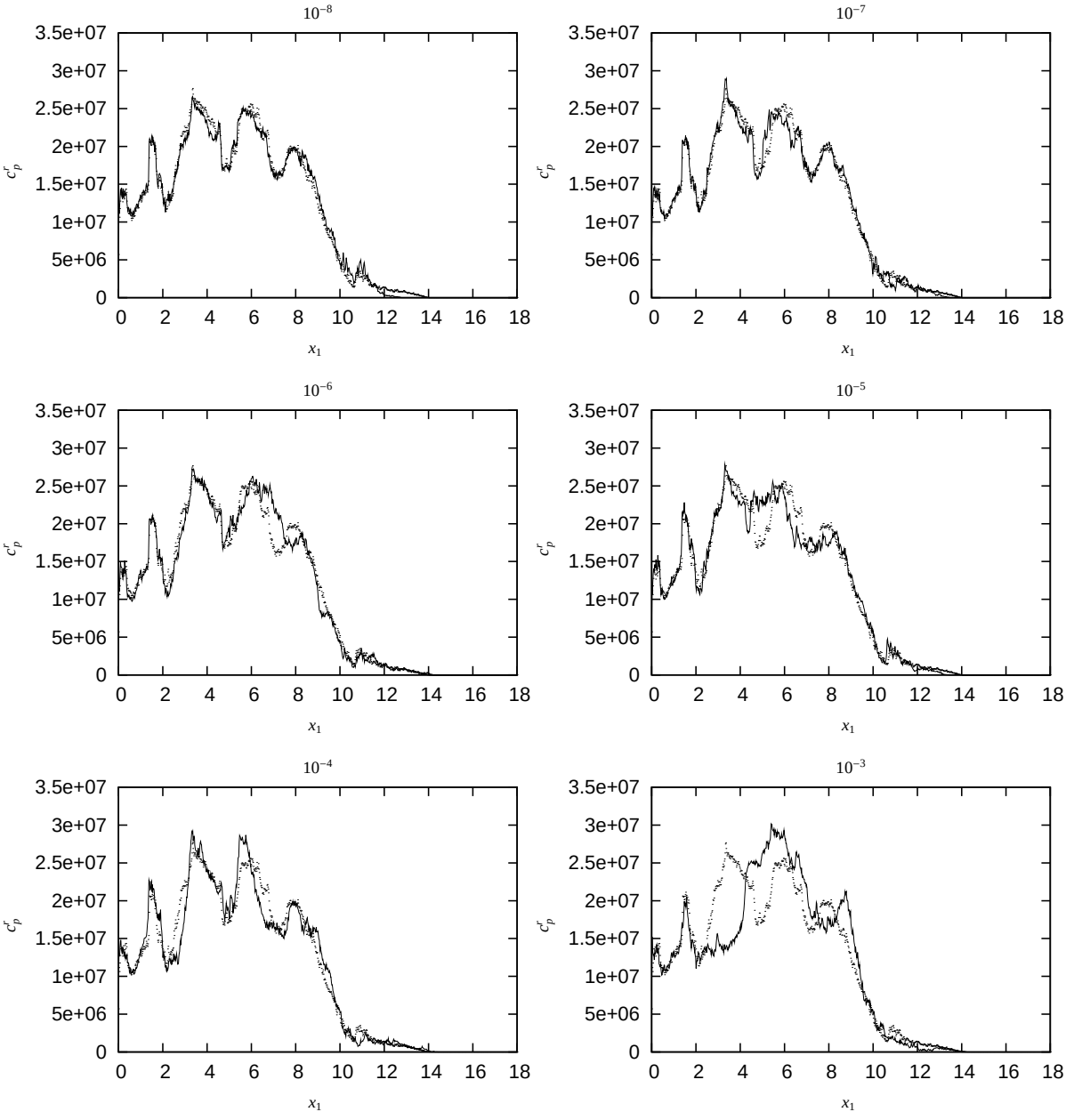

Figure 20: Final deposits at $t = 100$ of the simulations with superimposed noise (solid) and without noise (points).

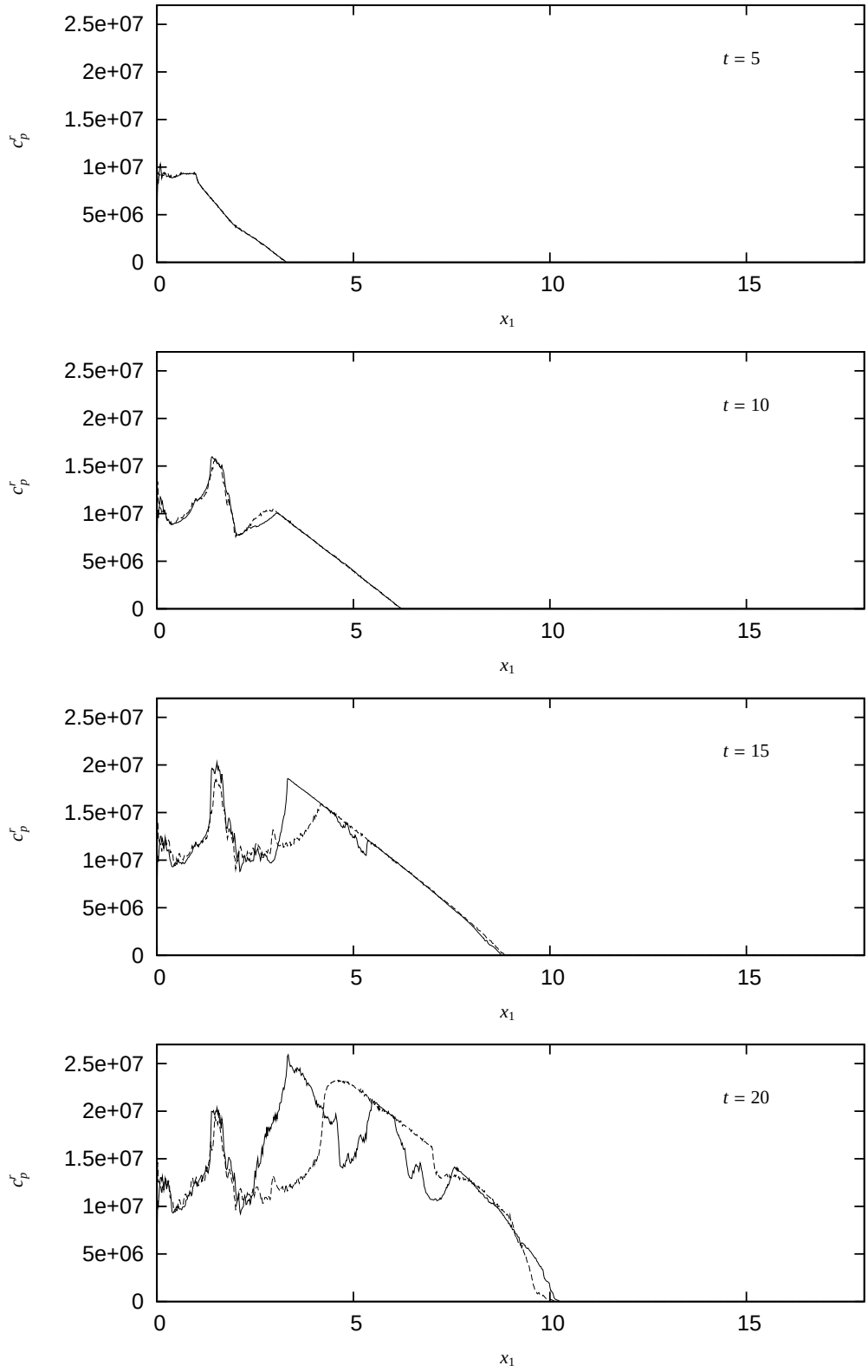

Figure 21: Deposit evolution of the simulation with noise amplitude 10^{-3} (dashed) and of the reference without noise (solid).

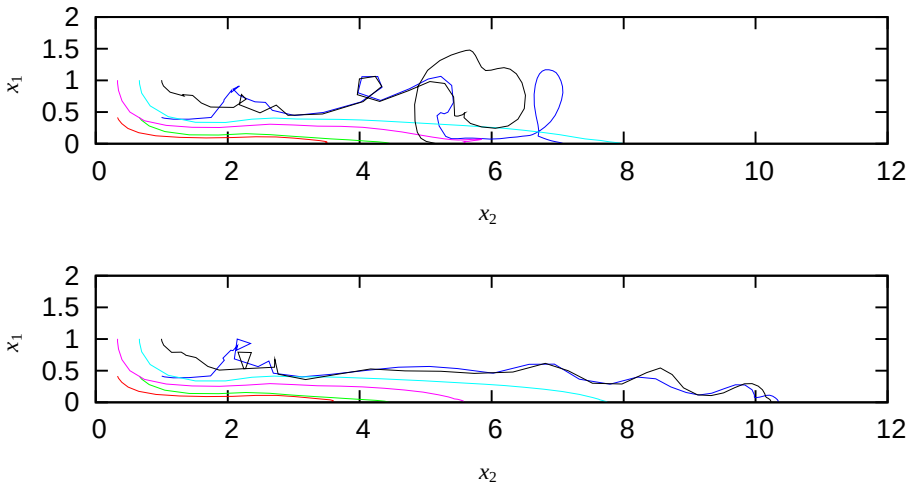

Figure 22: Particle paths with a resolution of $\Delta t = 0.5$ of six selected particles for the reference simulation (top) and the one with noise amplitude 10^{-3} (bottom).

3.2 Particles with inertia

Figure 23 shows a sequence of scatter-plots of a particle simulation with $St = 0.01$, i.e. we solve the equations (2.5) and (2.17) rather than (2.19) and (2.20) as in the previously presented particle simulations. We use the grid resolution 2049×513, the ratio $M = 100$ and the domain length $L_1 = 18$. We only simulate up till $t = 80$ rather than $t = 100$ like for the particles with negligible inertia as simulations with particle inertia take more time to run. Figures 24 and 25 compare the integral quantities of this simulation to the simulation of particles with negligible inertia and identical grid resolution and ratio M shown in figure 8.

Looking at figure 24, we see that in the early stage the mass of suspended particles and the front position both take similar values for both simulations. In the energy plots, we see that the phase of fast decrease in potential and fast increase of kinetic energy lasts longer for $St = 0.01$. But the kinetic energy of the fluid is lower for $St = 0.01$, as the kinetic energy of the particles is not negligible anymore. After the fast increase, the kinetic energy decays more slowly. As the kinetic energy of the particles decreases as well and the kinetic energy of the settling particles is negligible, i.e. Q_p is nearly zero, we can conclude that most of the kinetic energy of the particles is converted into kinetic energy of the fluid. The curves for the potential and the kinetic energy of the fluid are less wiggly, which could indicate a damping effect due to the inertia of the particles.

In figure 25 we see that the slopes of the mass of suspended particles and the front position change later and more abruptly for $St = 0.01$. In the energy plots, we see that less energy is dissipated by the Stokes flow around the particles and more by the resolved scales, i.e E_s is smaller and E_d is larger for the simulation with $St = 0.01$. We can also see that we have a larger energy loss in the system which we have found to be an indicator for a too coarse grid for the particles with negligible inertia. We calculate the relative energy loss for the simulation with $St = 0.01$ at $t = 20$ to be $5 \cdot 10^{-3}$. This is comparable to the loss for the coarser grid of the simulations with negligible particle inertia ($6 \cdot 10^{-3}$), where we have found the solution to improve after refining the grid.

Figure 26 shows a sequence of scatter-plots of a particle simulation with $St = 0.1$, grid resolution 2049×513 and ratio $M = 100$. It differs substantially from all previous simulations with smaller particle inertia. The initial column of particles sinks much slower. Later on, the height of the front is much smaller and we see less Kelvin-Helmholtz vortices forming.

Figure 27 compares the integral quantities of the simulation with $St = 0.1$ to the simulation with negligible particle inertia. We see that the suspend particle mass decays much faster. The front travels slower at first, but then catches up and at $t = 20$ is almost at the same position as the reference with negligible particle inertia.

In the energy plots, we see that the curves for the simulation with $St = 0.1$ are hardly wiggly, what could confirm our assumption of the particle inertia having a damping effect. The potential energy initially decays slower than for the reference, but for $t \gtrsim 5$ it is lower and at $t = 20$ there is hardly any potential energy left. A lot more of the potential energy is converted to kinetic energy of the particles than to kinetic energy of the fluid. At $t = 20$, the particles hardly have any kinetic energy and the kinetic energy of the fluid is significantly lower than for the reference. Instead, more energy is dissipated, especially by the Stokes flow around the particles. We also see that the kinetic energy of the particles leaving the domain is not negligible anymore, i.e. $Q_p \neq 0$.

We also observe that there is a gain in total energy for the simulation with $St = 0.1$. We calculate the relative energy gain at $t = 20$ to be $1.4 \cdot 10^{-2}$. Considering the previous simulations

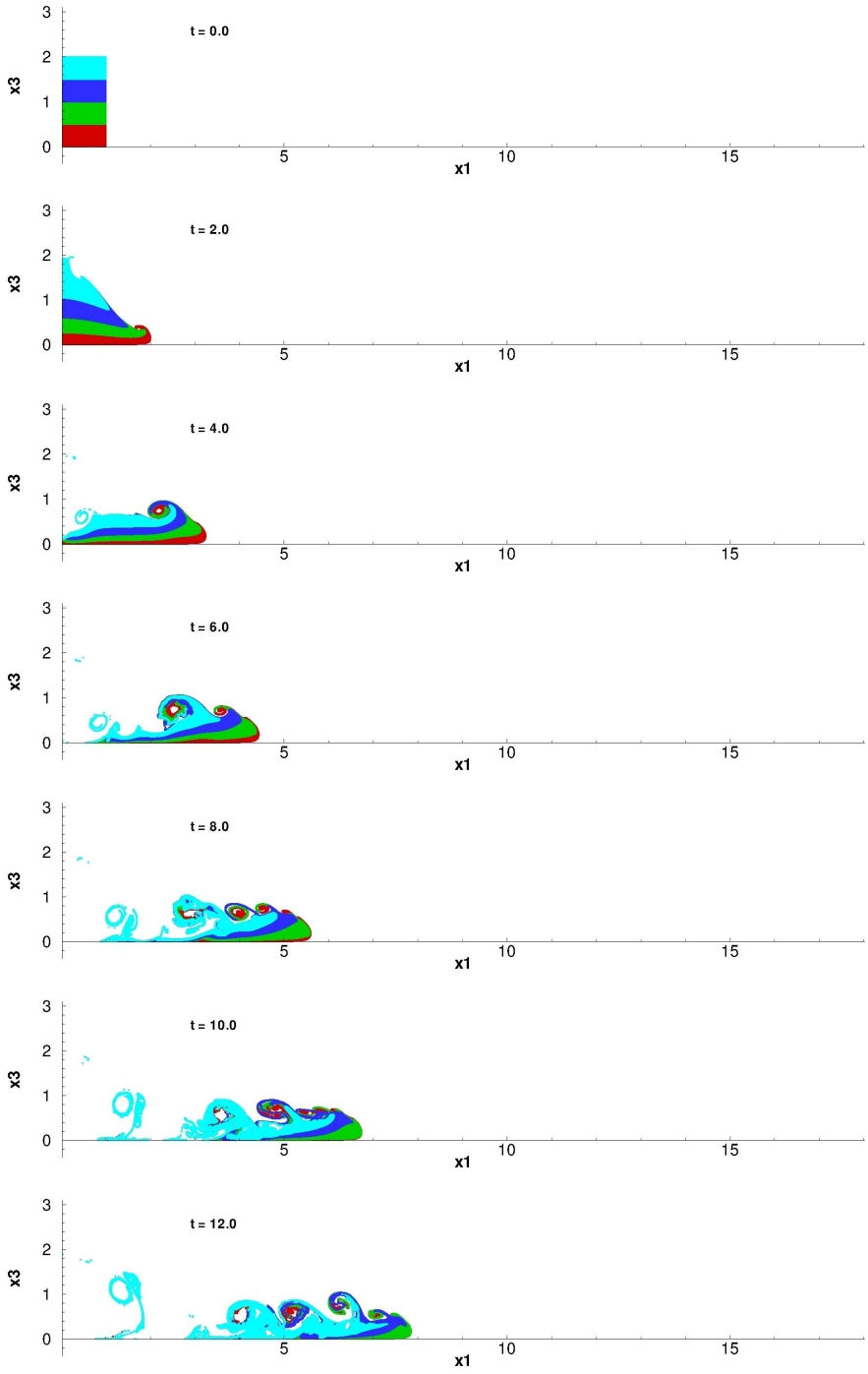

Figure 23: Scatter-plots of particles with Stokes number $St = 0.01$ with domain length $L_1 = 18$, grid resolution 2049×513 and real to computational particles ratio $M = 100$.

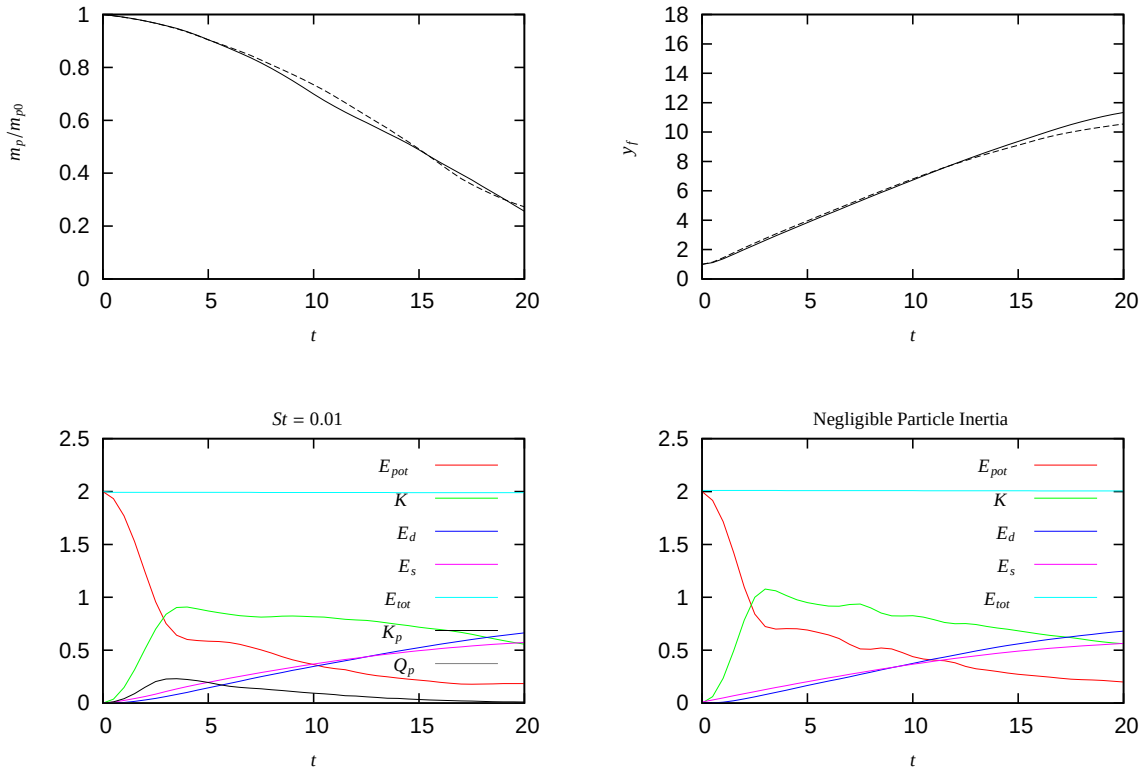

Figure 24: Integral quantities of the particle simulation with $St = 0.01$ in figure 23 (solid and bottom left) and the particle simulation with negligible inertia in figure 8 (dashed and bottom right) for $0 \leq t \leq 20$.

with identical grid resolution and ratio M, we have observed an energy loss of $5 \cdot 10^{-3}$ for the simulation with $St = 0.01$ and of $2 \cdot 10^{-3}$ for the simulation with negligible particle inertia. For the grid refinement study in section 3.1, we have found the energy loss to decrease if the grid is refined. We find the same to be true for the energy gain for simulations with $St = 0.1$, as illustrated in figure 28 which shows the energy plots for two simulations with $St = 0.1$ and $M = 100$, but different grid resolutions. If we assume the magnitude of the energy error to make a statement about how much too coarse the grid is, we can conclude that larger Stokes numbers require finer grids than smaller Stokes numbers, as for the same grid resolution the magnitude of the error is smaller for smaller Stokes numbers. Elghobashi and Truesdell [6] have found a decrease of the Kolmogorov scales for small particles in homogeneous decaying turbulence due to an increase of the dissipation rate. They have also found this effect to increase for larger particle response times [6], i.e. for larger Stokes numbers. For the simulation with $St = 0.1$, we find no dependence of the energy gain on neither the time step nor the ratio M.

Figures 29 and 30 show the deposit evolution of the simulation with $St = 0.01$ and the corresponding scatter-plots. In figure 29 we see the same almost linear decrease on the right as in the case with negligible inertia. We calculate the slope according to equation (3.11) at $t = 10$ for $4 \leq x_1 \leq 6$ to be $-3.22 \cdot 10^6$ and measure $-3.29 \cdot 10^6$. This is a slightly worse agreement than we find for the particles with negligible inertia.

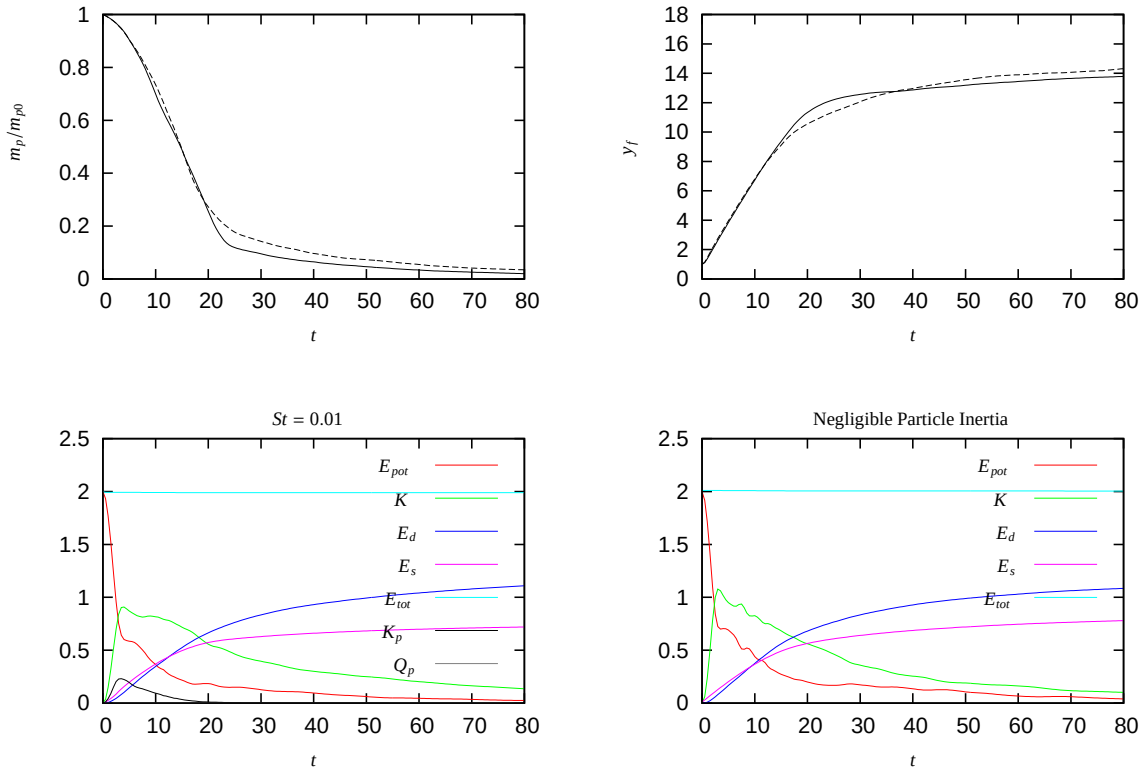

Figure 25: Integral quantities of the particle simulation with $St = 0.01$ in figure 23 (solid and bottom left) and the particle simulation with negligible inertia in figure 8 (dashed and bottom right) for $0 \leq t \leq 80$.

We also see the first dint forming at the same time as for the particles with neglected inertia, but it is much narrower. The first peak forms right at the end of the reservoir and again is much narrower than for negligible particle inertia. For the deposit at $t = 12$, there are more and smaller peaks to the right of the first large peak at $x_1 \approx 1$ than for the particles with negligible inertia. This could be due to more and smaller large scale vortices, which is hard to verify in the presented scatter-plots. From the final deposit in figure 31 at $t = 80$, we see the effect of the later and more abrupt change in the slopes of the mass of suspended particles and the front position around $t \approx 20$. The last peak appears later and the following drop off is steeper than for the particles with negligible inertia.

Figure 32 shows the evolution of the deposit for the simulation with $St = 0.1$ in figure 26. There is only a minor dip forming around $t \gtrsim 8$ at the beginning of the domain, followed by a minor peak downstream. We calculate the slope of the deposit at $t = 12$ for $4 \leq x_1 \leq 7$ according to equation (3.11) to be $-3.60 \cdot 10^6$, and measure $-3.24 \cdot 10^6$. This is a larger deviation than we find for $St = 0.01$ and for negligible particle inertia.

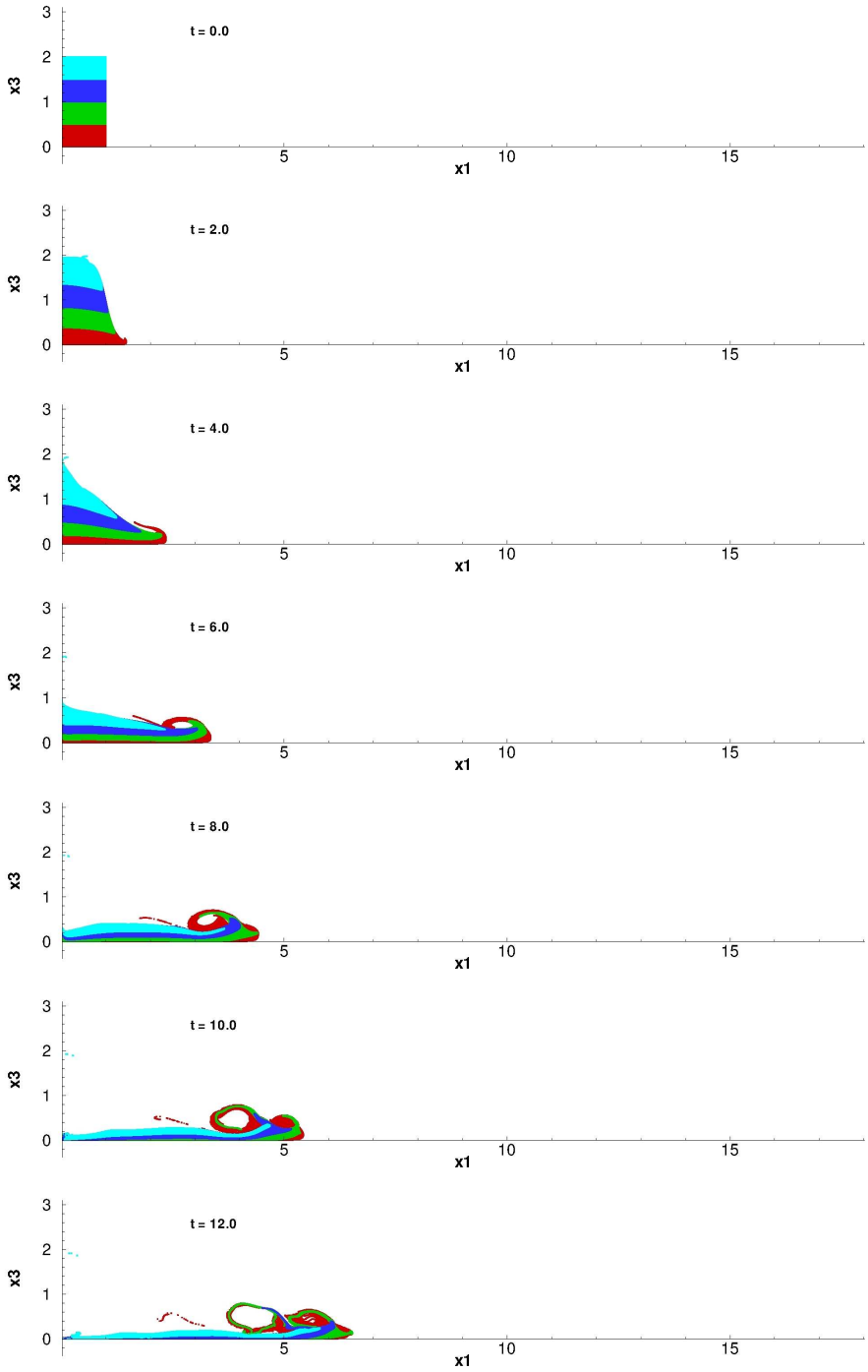

Figure 26: Scatter-plots of particles with Stokes number $St = 0.1$ with domain length $L_1 = 18$, grid resolution 2049×513 and real to computational particles ratio $M = 100$.

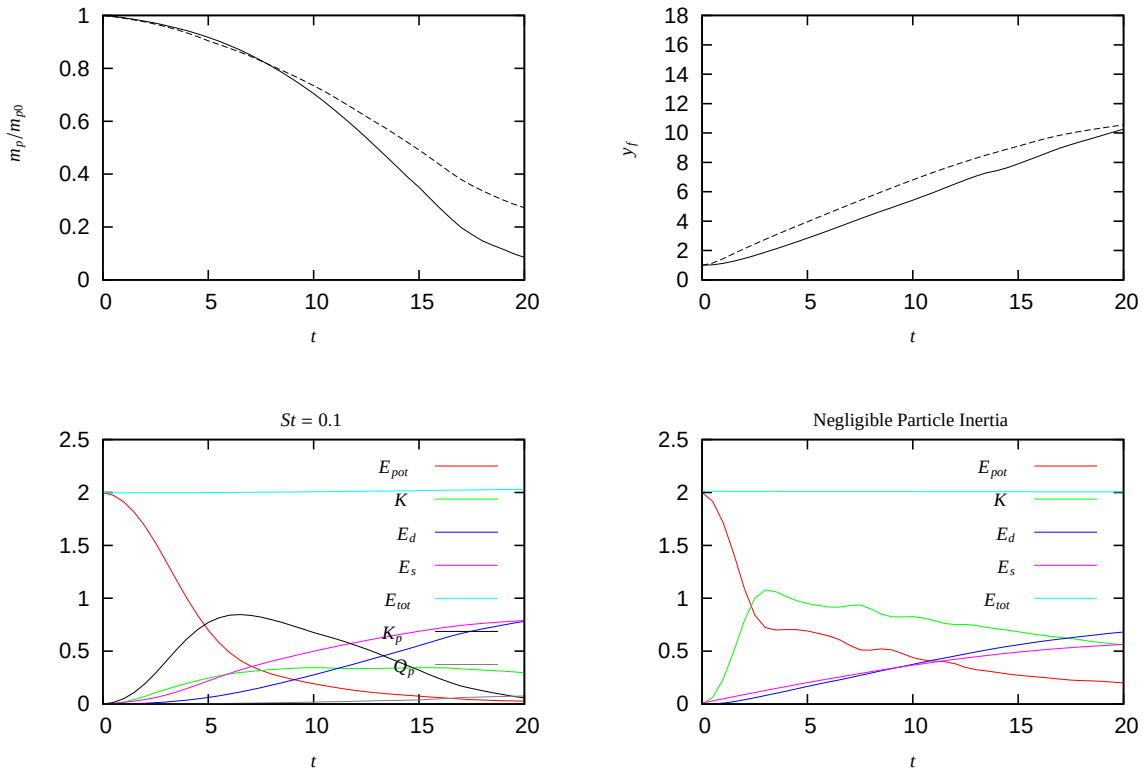

Figure 27: Integral quantities of a particle simulation with $St = 0.1$, grid resolution 2049×513 and $M = 100$ (solid and bottom left) and the particle simulation with negligible inertia in figure 8 (dashed and bottom right) for $0 \leq t \leq 20$.

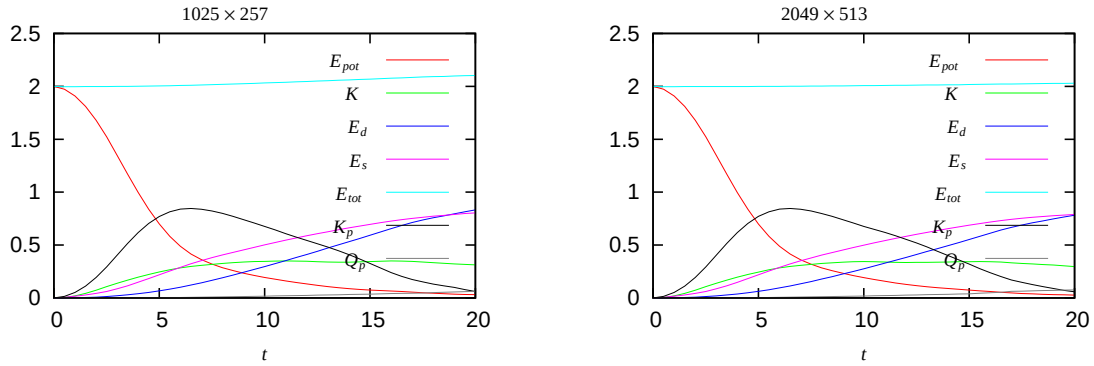

Figure 28: Comparing the energy plots of two simulations with $St = 0.1$ and two different grid resolutions.

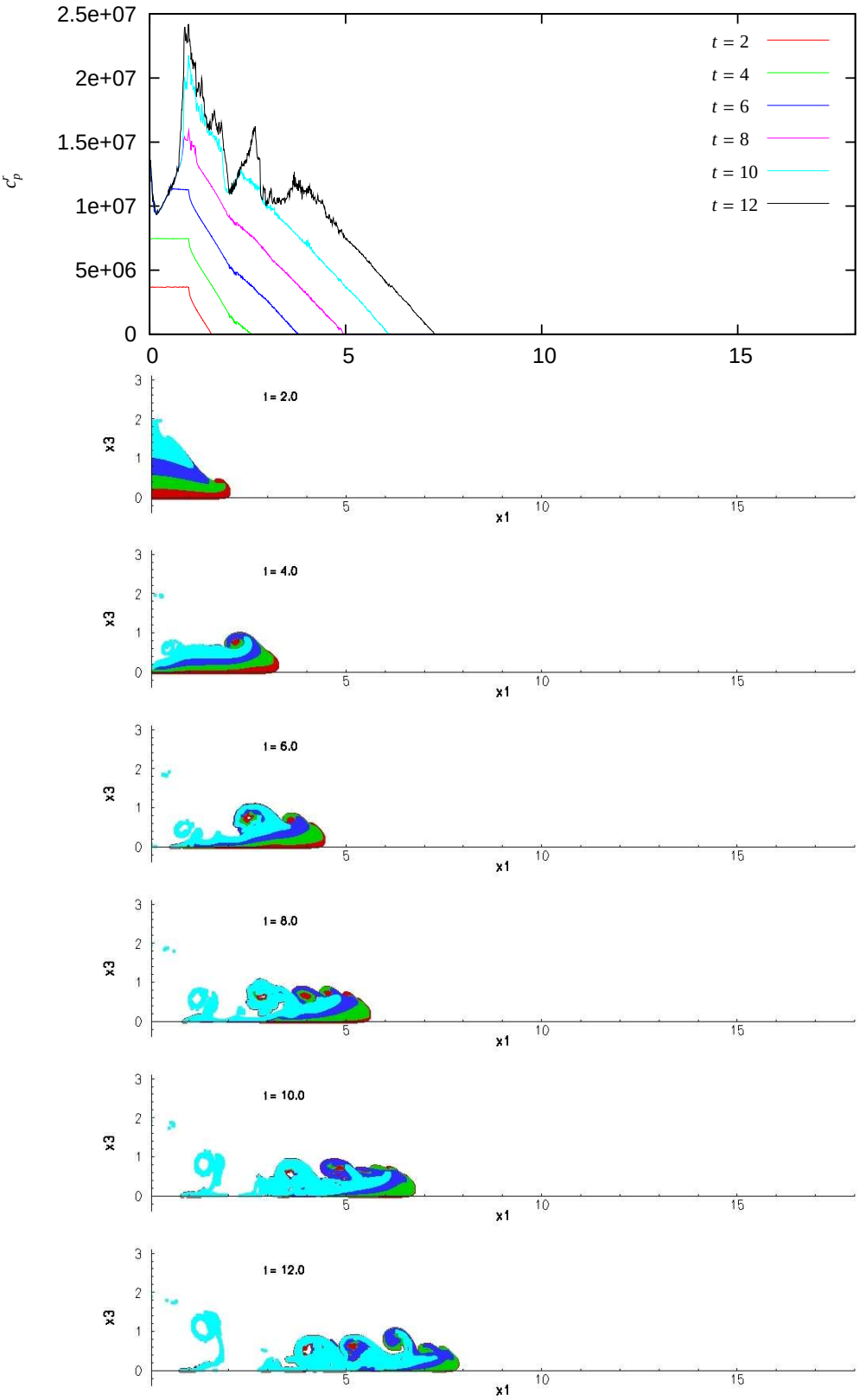

Figure 29: Deposit evolution and corresponding scatter-plots for the particle simulation with $St = 0.01$ in figure 23.

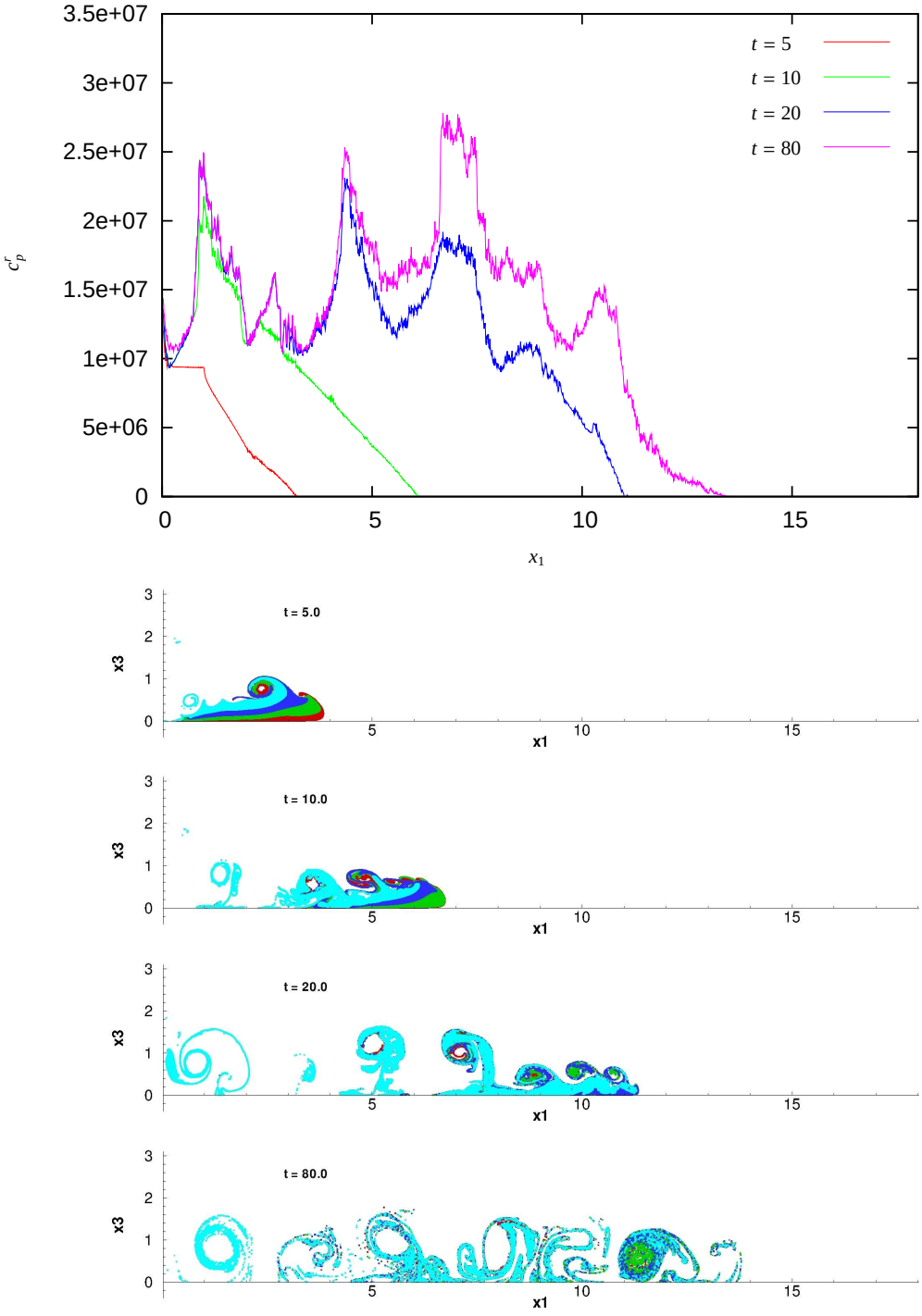

Figure 30: Deposit evolution and corresponding scatter-plots for the particle simulation with $St = 0.01$ in figure 23.

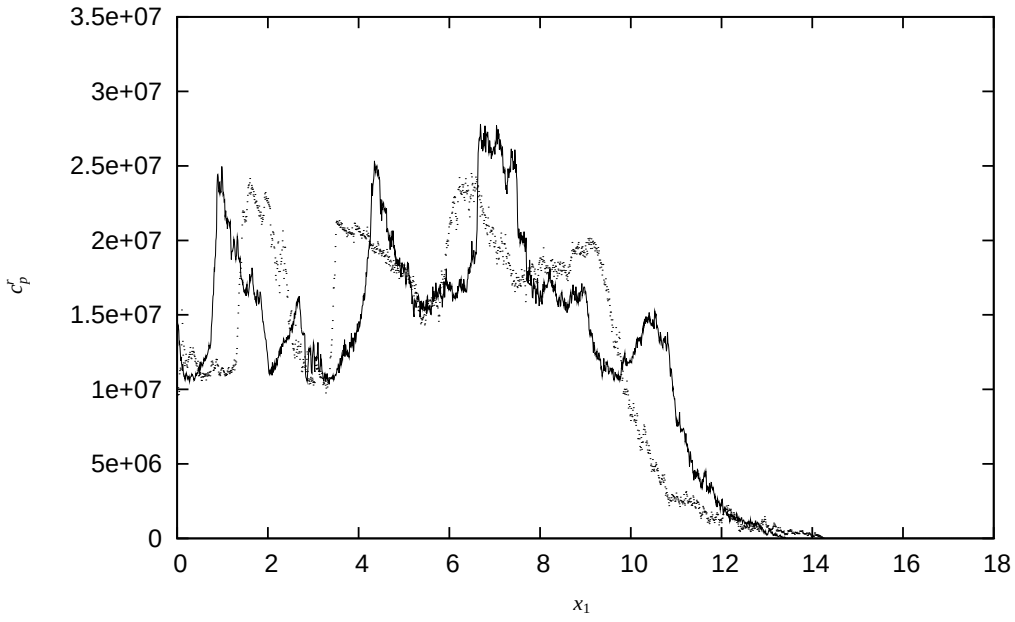

Figure 31: Final deposits at $t = 80$ for the particles with $St = 0.01$ (solid) and the particles with negligible inertia (dashed).

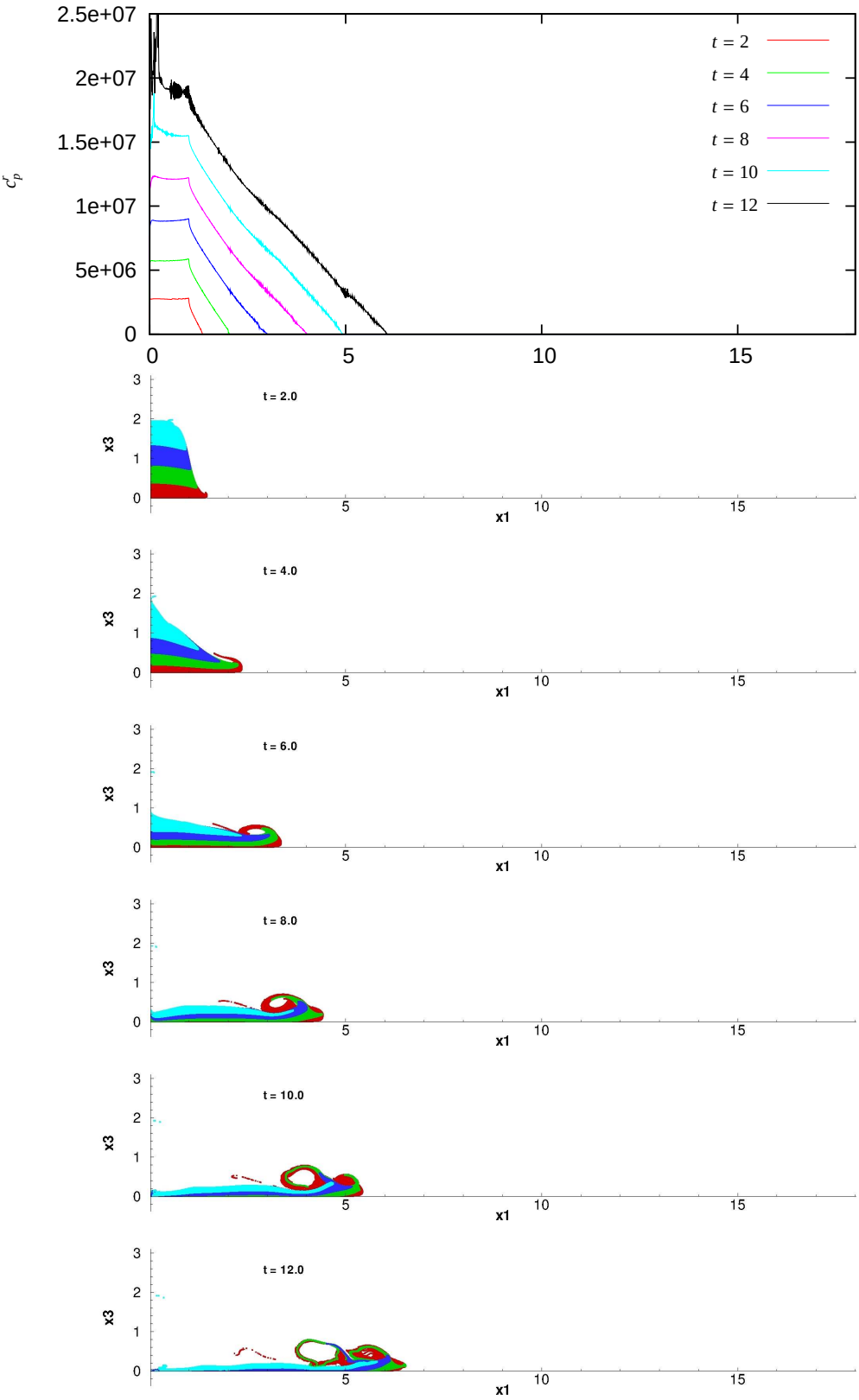

Figure 32: Deposit evolution and corresponding scatter-plots for the particle simulation with $St = 0.1$ in figure 26.

4 Concluding remarks and future work

We have derived the governing equations for particle driven gravity currents for small, spherical, monodisperse particles tracked in a Lagrangian manner. We only consider dilute suspensions as to neglect particle-particle interactions. The equations are available for particles with negligible and with inertia. Further, we make use of the concept of computational particles. We have derived the energy budget of the gravity current based on the governing equations. The equations are implemented in the IMPACT code by the IFD, where we use bilinear interpolation to determine the fluid velocity at the particle position and the tent function to distribute the particle feedback force on the fluid. We have also implemented algorithms to determine the mass of suspended particles in the domain, the front position and the deposit. We have performed 2D simulations with the Eulerian concentration approach for particles with negligible inertia and with the Lagrangian particle approach for both, particles with negligible and with inertia. The parameters are chosen in order to match the simulations by Necker [8] as close as possible.

For the concentration approach, we find a good agreement with the results by Necker [8] for $Sc = 1$. By increasing the Schmidt number to $Sc = 10$, we find the particles to settle faster, the front to travel more slowly, and the dissipation to be dominated by the resolved scales rather than by the Stokes flow around the particles. For $Sc = 10$, we find the concentration approach to agree very well with the Lagrangian particle approach with negligible particle inertia. The slight differences we observe (i.e. a faster particle settlement, a lower front speed, more dissipation by the resolved fluid scales and less by the Stokes flow around the particles for the Lagrangian approach) are the same differences we observe for the concentration approach when we increase the Schmidt number. Thus we can conclude that these slight differences are most likely due to the Lagrangian approach not containing any diffusion.

The grid refinement study for the particles with neglected inertia shows that the relative energy loss of the system is a good indicator to determine if the flow is adequately resolved. For the very coarse grids with few particles, we find the relative energy loss to depend on both the grid resolution and the ratio of real to computational particles M. For the finer grid resolutions, we find no visible dependence of the relative energy loss on the ratio M.

We find that the instantaneous forming of the Kelvin-Helmholtz vortices, especially further downstream, is highly sensitive to the initial particle distribution in the reservoir. We also find that these vortices are responsible for the dints and peaks in the deposit plots due to entrainment of clear fluid into the current. Taking this into account, there is a good agreement in the deposits for the particle and the concentration approach.

We present two simulations where particle inertia is considered. We find that as the Stokes number is increased, the relative energy error increases as well, indicating that larger Stokes numbers require a finer grid resolution. This is in good agreement with the findings by Elghobashi and Truesdell [6]. We also find that the potential energy and the kinetic energy of the fluid become less wiggly if the Stokes number is increased. We interpret this as a damping effect of the particle inertia. Also, we observe a faster settling of the particles for increasing Stokes numbers. Compared to the simulations with negligible inertia, the kinetic energy of the fluid is lower due to the presence of kinetic energy of the particles. We find that as the kinetic energy of the particles decays, it is mainly converted into kinetic energy of the fluid.

Regarding future work, it would be helpful to determine and write out the local particle volume fraction. This would simplify the comparison with the concentration approach. For the particles with resolved inertia, it could be used to check if particle-particle interactions

are negligible and would help to determine effects of particle accumulation and dilution when evaluating the results.

For the relative energy loss analysis in figure 14, we find a strong dependence of the energy loss on the number of particles. It might be interesting to investigate if more sophisticated interpolation schemes for determining the fluid velocity at the particle position and/or a different filter function for distributing the particle feedback force on the grid of the fluid have a positive influence on the solution. Balachandar and Maxey [2] investigated different interpolation schemes and found that for turbulent single particle dispersion, all but the trilinear interpolation give the same results and propose using Lagrangian interpolation scheme for single particle statistics due to it being the fastest after the linear interpolation.

From the two simulations with particle inertia, we see some tendencies for increasing Stokes numbers. But the differences between the results for the two Stokes numbers presented are significant. For a deeper insight, it would be helpful to perform more simulations with different Stokes numbers. Especially important would be to determine for which Stokes numbers we can neglect particle inertia without hesitation, as this reduces the computational cost significantly.

Our findings are solely based on 2D simulations and should be seen as the groundwork for 3D simulations. These should be performed, and the findings for the 2D case should be verified. For example, Necker [8] found no influence of larger Schmidt numbers for the concentration approach, which does not agree with our findings. This could be due to differences in the 2D and the 3D case.

For particles with negligible inertia, we find the computational cost for the Lagrangian particle approach to be much higher than for the Eulerian concentration approach, but do not find any significant differences in the results. If it is found that 3D simulations with particle inertia are not feasible or not efficient using the Lagrangian particle approach, it could be helpful to look into different approaches, for example the two-fluid approach as described in [4].

References

[1] A. Aliseda, A. Cartellier, F. Hainaux, and J.C. Lasheras. “Effect of preferential concentration on the settling velocity of heavy particles in homogeneous isotropic turbulence.” In: *J. Fluid Mech.* 468 (2002), pp. 77–105.

[2] S. Balachandar and M.R. Maxey. “Methods for Evaluating Fluid Velocities in Spectral Simulations of Turbulence”. In: *J. Comp. Phys.* 83 (1989), pp. 96–125.

[3] T. Bosse. “Numerical simulation of disperse two-phase flows”. PhD thesis. Zurich: Swiss Federal Institute of Technology, 2005.

[4] S. Elghobashi. “On Predicting Particle-Laden Turbulent Flows”. In: *Appl. Sc. Research* 52 (1993), pp. 309–329.

[5] S. Elghobashi. “Part 2: On the Approximation of the Two-Way Coupling Terms in the Trajectory Approach”. In: *Theoretical and Experimental Modeling of Particulate Flow*.

[6] S. Elghobashi and G.C.Truesdell. “On the two-way interaction between homogeneous turbulence and dispersed solid particles. I: Turbulence modification”. In: *Phys. of Fluids* A5 (1993), pp. 1790–1801.

[7] R. Henniger, D. Obrist, and L. Kleiser. “High-order accurate solution of the incompressible Navier-Stokes equations on massively parallel computers”. In: *J. Comp. Phys.* 229 (2010), pp. 3543–3572.

[8] F. Necker. “High-Resolution Simulations of Particle-Driven Gravity Currents”. PhD thesis. Zürich: Swiss Federal Institute of Technology, 2001.

[9] F. Necker, C. Härtel, L. Kleiser, and E. Meiburg. “Mixing and dissipation in particle-driven gravity currents”. In: *J. Fluid Mech.* 545 (2005), pp. 339–372.